AN ABSTRACT OF THESIS OF

Krista Kaiser for the degree of Master of Science in Radiation Health Physics

Presented on May 18, 2010.

Title: Performance Validation of a Prototype Skin Contamination Detector via Use of Very Thin Thermoluminescent Dosimetry.

Abstract approved:

David M. Hamby

The Nuclear Regulatory Commission (NRC) sets regulations for specific depths in the human skin for exposure to highly localized radioactive particles known as hot particles. This research determines the dose rate to a 10 cm^2 area with a density thickness of 1 mg/cm^2 at depths representing shallow dose, lens of the eye, deep dose, and other depths in the skin of biological interest, using experimental data obtained with very thin thermoluminescent dosimetry (TLDs). The TLDs are the thinnest LiF TLD-100s that are currently manufactured (0.3175 cm x 0.3175 cm x 0.0152 cm). The TLDs were irradiated on contact with radioactive sources to obtain data to construct calibration curves for each of the sources. The calibration curves were used to determine dose when layers of tissue-equivalent plastic were placed between the TLD and the source. Monte Carlo N Particle version 5 and VARSKIN version 3 computational code simulations were compared against the experimental data along with the prototypic skin contamination dosimeter, which was recently designed at Oregon State University.

Performance Validation of a Prototype Skin Contamination Detector via Use of Very Thin Thermoluminescent Dosimetry

by

Krista Kaiser

A THESIS

Submitted to

Oregon State University

in partial fulfillment of

the requirements for the

degree of

Master of Science

Present May 18, 2010

Commencement June 2010

Master of Science thesis of Krista Kaiser

presented on May 18, 2010.

APPROVED:

Major Professor, representing Radiation Health Physics

Head of the Department of Nuclear Engineering and Radiation Health Physics

---

Dean of the Graduate School

I understand that my thesis will become part of the permanent collection of Oregon State University libraries. My signature below authorizes release of my thesis to any reader upon request.

Krista Kaiser, Author

ACKNOWLEDGEMENTS

I would like to thank Dr. Camille Lodwick for all the MCNP help she graciously provided throughout the research project and Scott Menn for help with the TLD reader. I would like to thank Edward Cazalas for all of his help and input on the project. I sincerely thank my advisor Dr. David Hamby for his patience, guidance, and wisdom. I would also like to thank my friends and family who have always supported my academic endeavors. Last but not least, I would like to thank my parents who instilled a drive for academic achievement in me at a very young age.

TABLE OF CONTENTS

TABLE OF CONTENTS (Continued)

LIST OF FIGURES

LIST OF FIGURES (Continued)

LIST OF TABLES

LIST OF TABLES (Continued)

1.0 Introduction

The research performed as part of this thesis attempts to serve as a performance validation for a newly designed prototype skin contamination dosimeter. The skin dosimeter is envisioned to allow dose measurements at three depths of interest beneath the surface of the skin (Cazalas 2009). Current methods for determining skin dose include the computer program VARSKIN or the implementation of survey meters calibrated for such use. The objective of this research is to find the dose rate for select radionuclides at different skin depths to serve as validation for the prototype detector.

Regulations governing the protection of skin from exposure to radiation are set by the Nuclear Regulatory Commission in the Code of Federal Regulations, 10CFR20. The regulations require monitoring of shallow dose equivalent, deep dose equivalent, and dose to the lens of the eye. A major contribution to skin dose is from hot particles or extremely high localized doses to the skin. Hot particles are commonly found in nuclear waste cleanup sites, reprocessing facilities, and in both the primary and secondary support systems in nuclear reactors.

Very thin thermoluminescent dosimeters (TLDs) were used in this work to obtain dose rates at different skin depths. Plastic was used to achieve the desired density thickness to simulate skin depths. A variety of solid sources were used and liquid sources were attempted. The predicament of using liquid sources is explained in greater detail later in this report.

The computational code Monte Carlo N-Particle version 5 (MCNP5) was used to determine the dose rate from the radionuclide sources and as a benchmark for the experimental results. The experimental TLD data was compared against the computational code VARSKIN version 3, the prototype dosimeter, and a MCNP version 5 skin model.

2.0 Background Information

2.1 Skin Biological Review

The primary concern with hot particle exposure is the extremely high localized dose to the skin. The skin is divided into two primary sections - epidermis and dermis. The epidermis is further divided into several sections. The outer most region of the epidermis consists of 15 to 20 dead cell layers (ICRP 59). The dead cell layer is referred to as the stratum corneum and comprises approximately 25 percent of the total epidermis thickness; however, depending upon the location on the body, the stratum corneum may be thicker, such as the palms of the hands or the soles of the feet.

The stratum granulosum lies below the stratum corneum; this section is comprised of 4 to 5 layers of compressed cells with a degenerating nucleus. The cells of importance are located below the stratum granulosum. These cells are referred to as the stratum spinosum and the stratum germinativum. The stratum germinativum is also known as the basal layer. These layers provide the epidermis with structure and are highly radiosensitive. The effects of radiation induced damage will be manifested in these two regions (ICRP 59).

The dermis is further divided into two main sections: the papillary dermis and the reticular dermis. The papillary dermis is located under the stratum germinativum layer of the epidermis. The papillary dermis is the metabolically active region of the skin with the main purposes of thermoregulation and supporting the stratum germinativum layer. The reticular dermis is the primary structural component of the skin and is located under the papillary dermis. The total thickness of the dermis layer ranges from 1 to 3 mm depending upon the location on the body. Regions of the body, such as the back, have thicker dermis layers than the extremities (ICRP 59).

Highly localized dose from hot particles may occur from alpha, beta, or gamma radiation. Alpha radiation would be absorbed by the stratum corneum and is of minimal concern; however, an alpha particle with energy greater than approximately

6.5 MeV may penetrate the stratum corneum layer. The primary effect of highly localized dose is manifested in the form of an acute ulceration (ICRP 59). The size and depth of the ulcer is dependent upon the dose to the skin and the incident radiation energy.

Radiosensitive skin layers range from 50 μm to 100 μm in the epidermis, more specifically the basal cells. A value of 70 μm was selected as an average to be the standard for measuring shallow dose. Deterministic effects are most serious on dermal skin layers, ranging from 300 μm to 500 μm (ICRP 59).

2.2 Regulations

At the international level, radiation protection recommendations are presented by the International Commission on Radiation Protection (ICRP). In the United States, the Nuclear Regulatory Commission (NRC) adopted the recommendations in ICRP Publication 59: The Biological Basis for Dose Limitation in the Skin. Those regulations are stated in Title 10 of the Code of Federal Regulations Part 20.

The 10CRF20 states that the dose equivalent annual limit to the lens of the eye is 15 rem, shallow-dose equivalent is 50 rem averaged over 10 cm^2 to the skin of the whole body or to the skin of any extremity, and the deep-dose equivalent is 50 rem. The tissue depth at which the shallow-dose is to be monitored is 0.007 cm or 7 mg/cm^2. The tissue depth at which the deep-dose is monitored is to be 1 cm or 1000 mg/cm^2 and the tissue depth at which the lens of the eye is monitored is to be 0.3 cm or 300 mg/cm^2.

2.3 Hot Particles

Hot particles are highly radioactive particles, generally less than one millimeter in diameter. The activities range from a few Becquerel to magnitudes of 10^9 Becquerel. Hot particles are problematic in areas of contamination. The term “Nuclear Fuel Fleas” has been applied to hot particles from the nuclear power industry. Hot particles are found in the form of spallation nuclei from nuclear fuel. The high neutron flux in

nuclear reactors facilitates neutron activation of particles from impurities in the coolant due to corrosion of nuclear reactor structural materials.

The most common hot particle is Co-60. Other hot particles include mixed fission products, which may have escaped from the fuel element due to thermal expansion or fission gas buildup. The following is a list of other commonly encountered hot particle nuclides: ^{51}Cr, ^{54}Mn, ^{59}Fe, ^{89}Sr, ^{90}Sr, ^{90}Y, ^{95}Nb, ^{95}Zr, ^{103}Ru, ^{141}Ce, ^{144}Ce, and ^{144}Pr (NCRP 130).

2.4 Theory

2.4.1 Beta Decay Fundamentals

Beta decay occurs when a nucleus is energetically unstable due to its proportion of neutrons and protons. If the nucleus is neutron rich, then a neutron will transform into a proton and an electron, and the electron (beta particle) will be emitted. Beta particles are emitted with varying energy from essentially zero to a maximum value detailed by the nuclear makeup. Neutron rich nuclides are produced via neutron bombardment in areas of high neutron flux such as a nuclear reactor. Beta decay is not discrete and varies depending upon the atom undergoing radioactive decay. Beta decay is described by Eqn. (2.1) and gamma decay is described by Eqn. (2.2). A nuclide may or may not undergo gamma decay. The type of decay is characteristic of the nuclide.

$$ {}^{A}_{Z}X \rightarrow {}^{A}_{Z+1}Y + \beta^{-} + \bar{\nu} \tag{2.1} $$

$$ {}^{A}_{Z}X^{*} \rightarrow {}^{A}_{z}\mathrm{X} + \gamma \tag{2.2} $$

Beta decay includes the emission of an antineutrino to account for the difference in energy conservation and the energy of the beta particle. Energy and mass equivalence is given by Eqn. (2.3).

$$ E = mv^{2} \tag{2.3} $$

Given the relationship between mass, velocity, and energy, it is apparent why an antineutrino is required to balance the mass equation. A lower energy beta particle emission is accompanied with a high-velocity antineutrino and vice-versa since a neutrino has virtually no mass.

The maximum beta energy is equal to the Q-value of the decay reaction. The Q-value is the change in rest mass of the reaction. Eqns. (2.4) and (2.5) describe the relationship of kinetic energy and rest mass to the Q-value, respectively (Shultis 2002).

$$\text{Q-value} = (\text{Kinetic Energy of Final Particles}) - (\text{Kinetic Energy of Initial Particles}) \quad (2.4)$$

$$\text{Q-value} = (\text{Rest Mass of Final Particles})c^2 - (\text{Rest Mass of Initial Particles})c^2 \quad (2.5)$$

A simple radioactive decay equation can be expressed by Eqn. (2.6), where the parent nuclide is given by the variable X and the daughter is give by the variable Y. The smaller x and y notation represents the bombardment particle (or wave) and the decay particle (or wave), respectively.

$$X + x = Y + y \quad (2.6)$$

Eqn. (2.7) is the decay equation expressed in terms of kinetic energy and rest mass. The speed of light (c^2) is conveniently expressed as 931.5 MeV per atomic mass units (amu).

$$\text{Q-value} = (EY + Ey) - (EX - Ex) = [(MY + My) - (MX + Mx)]c^2 \quad (2.7)$$

The following (Eqn. (2.8)) is an example of a calculation for the Q-value for Co-60 decay.

$$^{60}_{27}Co \rightarrow ^{60}_{28}Ni + \beta^- + \bar{\nu} \quad (2.8)$$

The following are the atomic mass units for each nuclide and the beta particle.

$$^{60}_{27}Co = 59.933817 amu$$

$$^{60}_{28}Ni = 59.930786amu$$

$$\beta = 5.4857990943E-4amu$$

To obtain the maximum beta energy, the antineutrino is assumed to have zero energy. In order to conserve charge, 2 electrons are added to the parent side of the equation as seen in Eqn. (2.9).

$$Q-value = \left[(m(^{60}_{27}Co) + 2e^{-}) - (m(^{60}_{28}Ni) + m(\beta) + m(\bar{\nu}))\right]c^2 \quad (2.9)$$

Substituting the atomic mass, as seen in Eqn. (2.10), a Q-value of 0.00358 amu is obtained. Multiplied by the 931.5 MeV per amu, the Q-value becomes 3.33 MeV.

$$Q-value = \left[(59.933817 + 2(5.4857990943E-4)) - (59.930786 + (5.4857990943E-4) + 0)\right]c^2 \quad (2.10)$$

A Q-value of 3.33 MeV accounts for both the nuclear mass and the atomic mass. To obtain only the nuclear mass, 0.511 MeV is subtracted from the Q-value, thus a Q-value of 2.82 MeV is obtained. The maximum beta possible would have an endpoint energy of 2.82 MeV, however Co-60 emits two gamma rays with energies 1.3325 and 1.1732 MeV (see Figure 2-1). Two beta decay routes are possible followed by further gamma emission to reach a stable state.

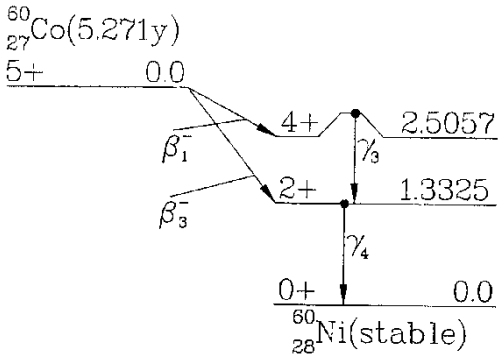

Figure 2-1: Co-60 decay scheme (ICRP 38)

The endpoint energies for the beta particles are obtained from the maximum beta energy minus the energy state in which a gamma ray is emitted. Therefore, 2.819

minus 2.5057 equals a 0.3133 MeV beta and 2.819 minus 1.3325 equals a 1.4865 MeV beta. However, each beta decay route has a certain probability associated with it, therefore the decay of a maximum beta of 0.3133 MeV to energy state of 2.5057 will yield two gammas, the first with an energy of 1.1732 MeV and the second with an energy of 1.3325 MeV. This path in the decay scheme has a probability of occurrence of 99.9 percent, whereas the alternative path of a maximum beta of 1.4865 and one gamma ray of 1.3325 MeV has a probability of only 0.08 percent.

The mean beta energy is found from the sum of the beta energies multiplied by their intensity. Co-60 has two average energies associated with the two endpoint energies, therefore the mean average energy is found by Eqn. (2.11).

$$\sum\left[(95.77\times.9988)+(625.87\times0.0012)\right]=96.4061keV \tag{2.11}$$

2.4.1 Beta Particle Interactions

The range (in mg/cm^2) of the beta particles as a function of energy (MeV) is approximated by the empirical fit defined by Eqn. (2.12) (Martin 2006). Table 2-1 provides the range of the maximum beta particle emitted by the five sources used in this research.

$$Range = 412\times E_{max}{}^{(1.265-0.00954\times\ln(E_{max}))} \tag{2.12}$$

Table 2-1: Range of beta particles

Nuclide	Range [mg/cm^2]
C-14	38
Co-60	682
Cs-137	505
Sr-90	191
Y-90	1161

Electrons lose energy by creating ionizations in the surrounding material. The incident electron dislodges orbital electrons due to the Coulombic forces, thus creating ion pairs (Martin 2006). The electrons created from the initial ionization may also produce an ion pair. The ejected secondary electron is referred to as a delta ray if it

has sufficient energy to create further ionization. Due to the lower energies of the particles, most of the energy is absorbed locally. Electrons may change direction due to deflection from the nucleus. This change in direction is accompanied by energy loss in the form of a photon. This process is known as bremsstrahlung.

The energy loss from excitation and ionization is referred to as collisional energy loss and the energy loss from bremsstrahlung is referred to as radiative energy loss. Eqn. (2.13) is used to calculate the collision stopping power - (Eqns. 2.14 – 2.16) are supporting equations (Turner 2007), where T is the incident beta particle energy in MeV. The variable 'n' is the electron density expressed as total electrons per m^3.

$$\left(\frac{-\partial E}{\partial x}\right)_{Col} = \frac{(5.08E{-}31)\times n}{\beta^2}\left[G(\beta) - \ln(I)\right] \tag{2.13}$$

$$G(\beta) = \ln\left(3.61E5 \times \tau\sqrt{\tau+2}\right) + F^{-}(\beta) \tag{2.14}$$

$$F^{-}(\beta) = \frac{1-\beta^2}{2}\left[1 + \frac{\tau^2}{8} - (2\tau+1)\ln(2)\right], where\ \tau = \frac{T}{mc^2} \tag{2.15}$$

$$\beta^2 = \frac{T\times(T+1.022)}{(T+.511)^2} \tag{2.16}$$

To relate radiative stopping power to collisional stopping power Eqn. (2.17) is used (Tuner 2007). Near tissue equivalent plastics were used in this research; therefore, the radiative loss is negligible due to the very low Z values of the plastic and relatively low energies of the beta particles emitted.

$$\frac{\left(\frac{-\partial E}{\partial x}\right)_{RAd}}{\left(\frac{-\partial E}{\partial x}\right)_{Col}} \cong \frac{ZE}{800} \tag{2.17}$$

The Bragg peaks were calculated and graphed for a Cs-137 button source with electrons incident on a TLD chip with a lithium fluoride composition and for polyethylene (Figure 2-2). Polyethylene was used to simulate near tissue equivalent plastic. The Bragg peaks were calculated from the collisional stopping power (Eqns. 2.13 - 2.16). A visual basic program was written to handle the numerous iterations

required for determining the electron energy as it transverses the material in each finite element.

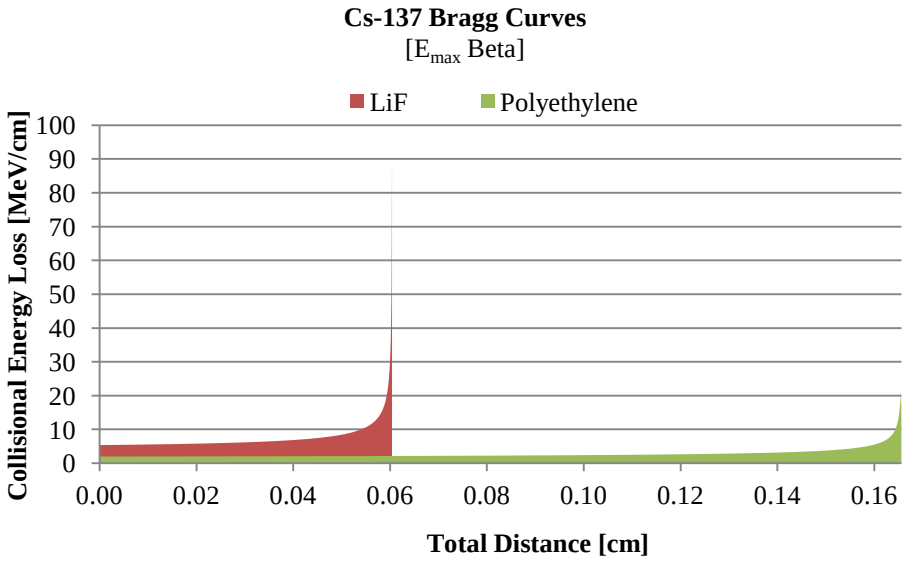

Figure 2-2: Bragg Curves

The collisional energy loss per unit distance is greater for the LiF TLD than the polyethylene due to the density and high Z value of the two compositions. The electrons penetrate farther and lose less energy through the polyethylene than through the LiF TLD.

2.4.2 Gamma Interactions

Photons interact and lose energy by inelastic scattering, also known as Compton scattering, pair production, and photoelectric absorption. Photoelectric absorption occurs when a photon interacts with an orbital electron, resulting in the ejection of the electron from the orbital and the photon being completely absorbed. The vacancy in the electron shell is filled by an outer shell electron dropping down. This process results in emission of a characteristic x-ray due to the decrease in energy state of the dropped electron.

Compton scatter occurs when a photon interacts with an orbital electron, resulting in the electron being ejected from the orbital and the photon scattering with a reduced

energy, thus leaving the atom ionized. The Eqn. (2.18) provides the scattered photon energy given a particle scatter angle. (Carron 2007).

$$E' = hv' = \frac{hv_o}{1+\alpha(1-cos\theta_\gamma)},\ where\ \alpha \equiv \frac{hv_o}{mc^2} \tag{2.18}$$

Pair production occurs when a photon with energy greater than 1.022 MeV passes near a nucleus and spontaneously disappears and a positron-electron pair emerge due to the static electric field surrounding either the nucleus or electron. The positron and the electron will lose energy via inelastic scatter and bremsstrahlung. Once the positron has exhausted all of its kinetic energy, it will combine with an electron and will result in the emission of annihilation radiation of two photons in opposite directions, each 0.511 MeV.

2.4.3 Conversion Electron

Conversion electrons result when the nucleus transfers its excitation energy to an orbiting electron instead of a gamma-ray, resulting in the ejection of the electron. Conversion electrons have discrete energies based upon the difference in energy between the nuclear excitation energy and binding energy of the orbital electron. Conversion electrons may produce bremsstrahlung due to their typically high energies.

The decay of Cs-137 results in a prominent conversion electron with a yield of 7.79 percent and energy of 0.624 MeV; therefore, this conversion electron was included when determining skin dose from the Cs-137 source.

2.4.4 Dose Contributions

The dose contributions from gamma, beta, and conversion electron particles were modeled with MCNP to obtain the percentage contribution of total dose for each type of radiation. Figure 2-3 and 2-4 display the breakdown of dose contribution for Cs-137 and Co-60. Carbon-14, Sr-90, and Y-90 are pure beta emitters and the primary mode of decay for Ba-133 is isomeric transition. Figure 2-5 displays the breakdown of dose contribution from Sr-90 and its daughter nuclide Y-90.

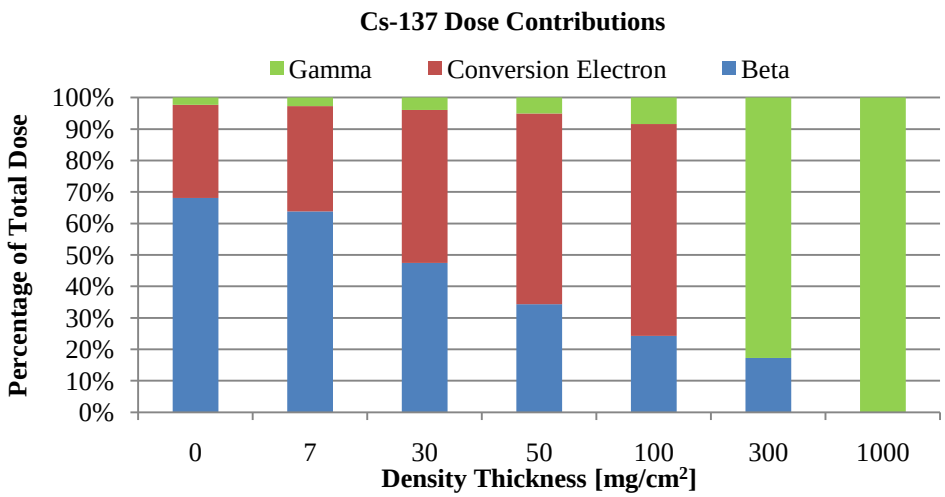

Figure 2-3: Cs-137 particle dose contributions

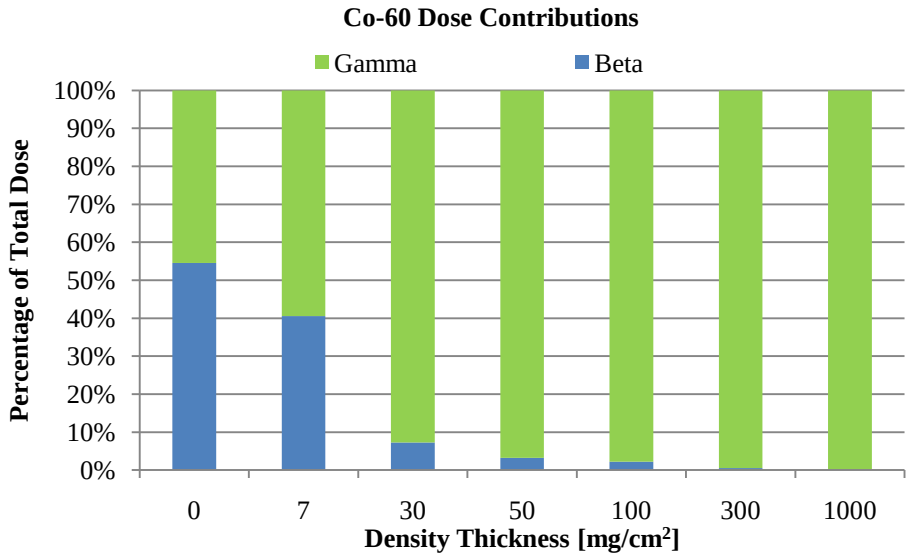

Figure 2-4: Co-60 particle dose contributions

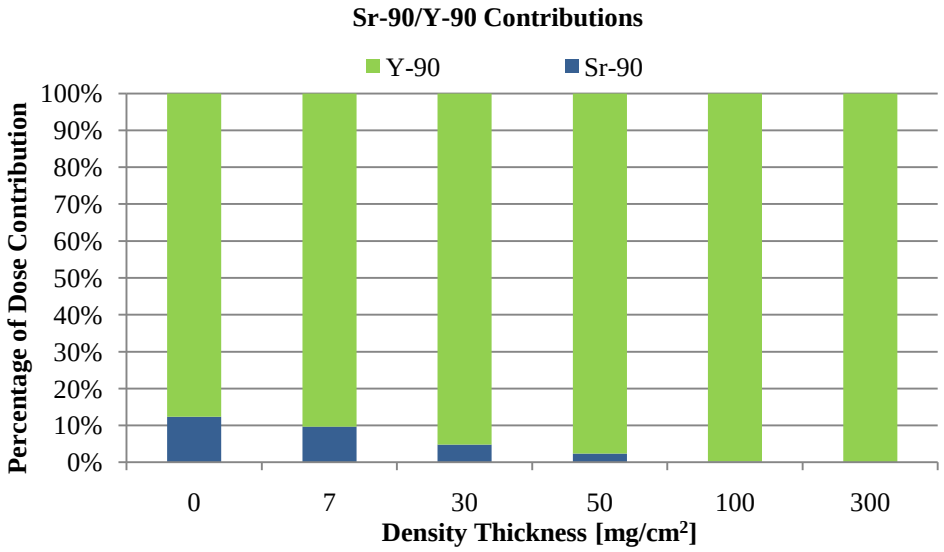

Figure 2-5: Sr-90/Y-90 dose contributions

2.4.5 Dose and KERMA

The basic definition of radiation absorbed dose is energy absorbed per unit mass of material. Radiation dose is measured in units of rad, defined as 100 ergs per gram, where 1 Joule is equivalent to 10^7 ergs. The SI unit of dose is the Gray (Gy) and is defined as 1 Joule per kilogram. The relationship between rad and Gray is defined as 1 Gray is equivalent to 100 rads.

Equivalent dose is defined as the product of absorbed dose and a radiation weighting factor. The radiation weighting factor for both photons and betas is currently assigned the value of unity. Effective dose is defined as the product of absorbed dose, radiation weighting factor, and a tissue weighting factor. The tissue weighting factors vary for each organ and are based on stochastic risk. Both the tissue weighting factors and the radiation weighting factors are set by the ICRP committee and vary between ICRP publications as more data on radiation risk is obtained.

KERMA is defined as kinetic energy released in matter and has the same units as dose; however, KERMA is the measure of energy transferred from uncharged particles i.e. X-rays, gamma rays, and fast neutrons to ionizing particles per unit mass (Cember 2009). The transfer of energy from uncharged particles to ionizing particles is not

necessarily a localized event and energy can be absorbed outside the volume in which it is transferred.

2.4.6 Charged Particle Equilibrium

Charged particle equilibrium (CPE) occurs when the energy flux of particles leaving the volume of interest is equal to the energy flux of particles entering the volume of interest. Figure 2-6 is a diagram of the relationship between KERMA and dose with depth of penetration in a given medium. As depicted in the figure, photons are entering a medium and interactions with atoms are occurring immediately. KERMA is directly proportional to the fluence of the photon beam; therefore, attenuation by the medium reduces the fluence exponentially. The photon interactions produce electrons which are the main contribution to dose near the surface of the medium. The dose builds up linearly as electrons continue to be produced, until the depth is equivalent to the range of the maximum electron. At this point, charged particle equilibrium has been met (Carron 2007). The KERMA depicted on the figure is KERMA due to collisional losses.

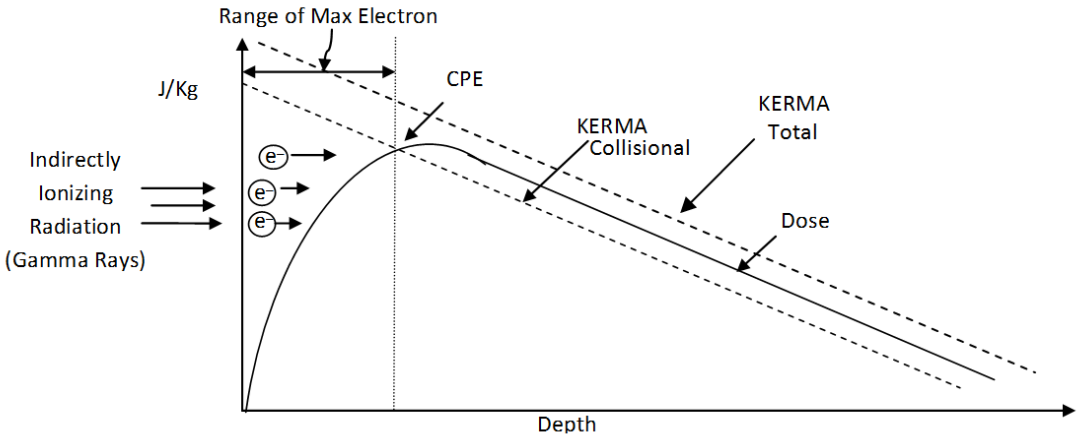

Figure 2-6: CPE diagram

Different material densities affect the KERMA, since the electron stopping powers are not equivalent. The effective Z of the LiF TLD is 8.2, which is reasonably close to the value for tissue (7.51). It is therefore assumed that the LiF TLD is near tissue-

equivalent, therefore CPE is established before reaching the TLD chip: otherwise the TLD chip could re-initiate a buildup region.

2.5 Thermoluminescent dosimeters

Thermoluminescent dosimeters (TLDs) are essentially crystals which store energy absorption data via crystalline electron displacement. Incident radiation excites an electron in a crystal lattice structure from the valance band to the conduction band. The region between the valance band and the conduction band is known as the band gap and electrons are forbidden in this region unless impurities or activators are added to the crystal. Once the electron has been excited to the conduction band it will want to de-excite to the valance band, which is a lower energy region. The electron will fall into the band gap and due to minimal energy will become trapped within the band gap region at activator sites. This trapped electron is essentially storing information regarding the radiation absorbed within the crystal. The electrons fall back to the valance band at a rate of approximately 10^{-8} to 10^{-7} percent per second – this is known as fade (Cember 2009).

To process a TLD, the crystal is placed in a TLD reader on a metal planchet strip. The TLD is heated to provide trapped electrons with sufficient energy to reach the conduction band again and to drop down to recombine with positive holes within the forbidden band gap at activator sites. As the electron recombines with a positive hole, the excess energy is emitted as a thermoluminescent photon. The band gap region is on the order of 3 to 4 eV; therefore, the emitted thermoluminescent photon is within the visible spectrum. This light is detected via a photomultiplier and a direct correlation is observed with the collected light intensity to the number of trapped electrons. Figure 2-7 depicts how the visible photons are created in a TLD crystalline structure.

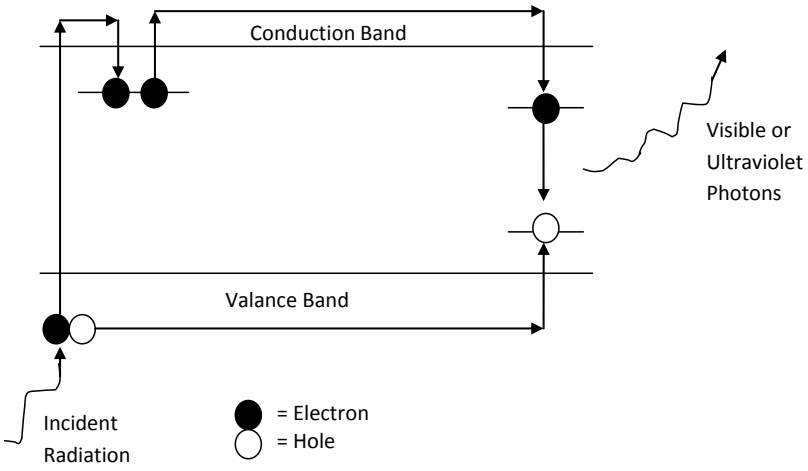

Figure 2-7: TLD crystal interactions

A glow curve is constructed from the TLD reader light output. The glow curve is a measure of the relative thermoluminescent photon intensity verses the applied temperature. The integration of the glow curve provides information regarding the total amount of trapped electrons (Knoll 2000). The TLD reader used for this research only provided a single digital output of the summed glow curve. Newer equipment would be required to analyze glow curve outputs.

The TLDs used in this research are type TLD-100s from ThermoFisher and are the thinnest TLD-100 chip manufactured. The TLD-100s are 0.3175 cm x 0.3175 cm x 0.01524 cm. The TLD-100s are made from a natural composition of LiF, with approximately 400 ppm of Mg and approximately 8 ppm of Ti (Knoll 2000). The natural composition of Li contains 92.5 percent ^{7}Li and 7.5 percent ^{6}Li. The density of the TLD-100s is 2.64 g/cm^{3}. The Z_{eff} of the TLD-100s are 8.2, which is reasonably close to 7.4, the Z_{eff} for water (Gad 1991). TLD-100s are sensitive in the range of 10^{-3} to 10^{5} R.

The TLD reader has three distinct heating regions: pre-irradiation anneal, post-irradiation anneal, and read. The pre-irradiation anneal effectively zeros the TLD chips. Figure 2-8 is a diagram of the heating regions in relation to a hypothetical glow-curve output.

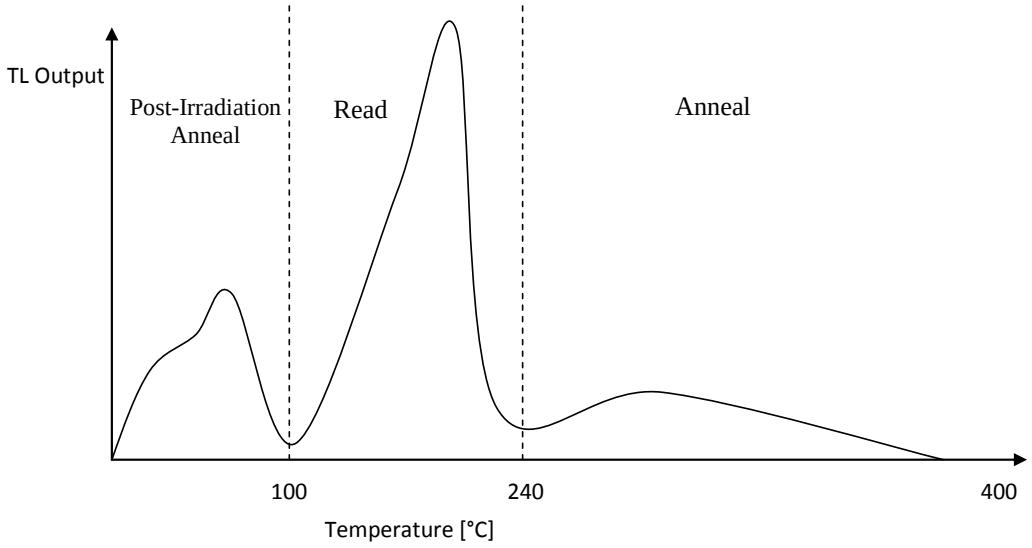

Figure 2-8: TLD heating regions relative to a glow curve output

The TLD-100s require a pre-irradiation anneal at 400 ºC for 1 hour and a post-irradiation anneal at 100 ºC for 10 minutes. The main glow peak for the TLD-100s is located at 195 ºC. The post-irradiation anneal is used to reduce the low-temperature dosimetry traps. The low-temperature peaks are quick to fade due to the limited amount of excess energy required to liberate the electrons. If a post-irradiation anneal is not performed, these low-temperature peaks are included in the readout and may overestimated the dose signal on the TLD chip.

2.6 TLD Readers

TLD readers work by heating the TLD chip and measuring the light output from the photon emissions via de-excitation of electrons trapped in the crystal's forbidden band. The TLD chip is placed on a planchet which is heated and measured via a thermocouple. The light emission is focused through a filter or wave shifter which serves to convert the emitted photon wave frequency to a visible spectrum photon which can then be collected in the photomultiplier tube (PMT). The PMT output (current) is then integrated over a set integration range, i.e. 100 ºC and 240 ºC. Figure 2-9 is a block diagram of the basic working of a TLD reader. The TLD reader used in this work is a Harshaw Model 2000 A/8.

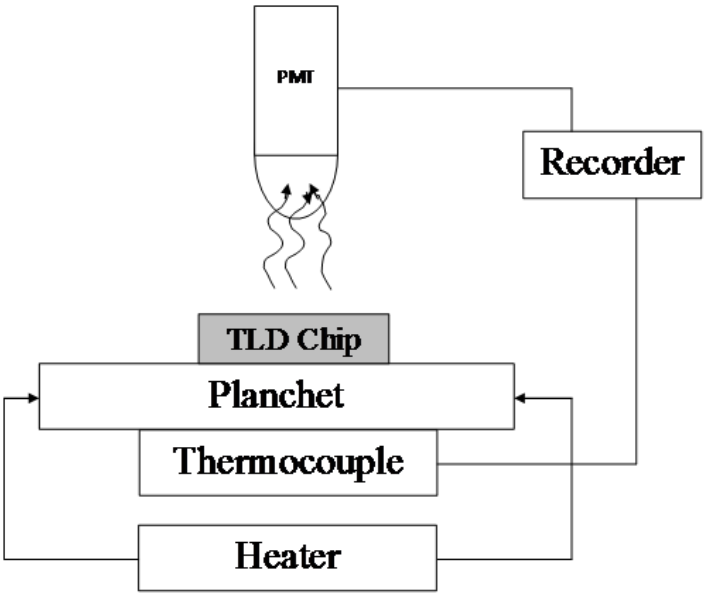

Figure 2-9: Block diagram of TLD reader

2.6.1 Photomultiplier Tubes

A photomultiplier tube is used to convert visible photons emitted from the TLD chip to an electrical signal. The photons interact with the photocathode, where the energy from the photons is absorbed into the photocathode material and is transferred to an electron. The freed electron migrates to and escapes from the surface of the photocathode. Subsequent electrons are then accelerated into the first dynode. The dynode material is designed such that energy deposited by an incident electron will result in the emission of more than one electron from the surface of the dynode. Photomultiplier tubes have about 10 dynodes. After multiplication through the dynode stages, the electrons are collected by the anode and the electrical signal is processed. Figure 2-10 illustrates the process of electron multiplication in a photomultiplier tube.

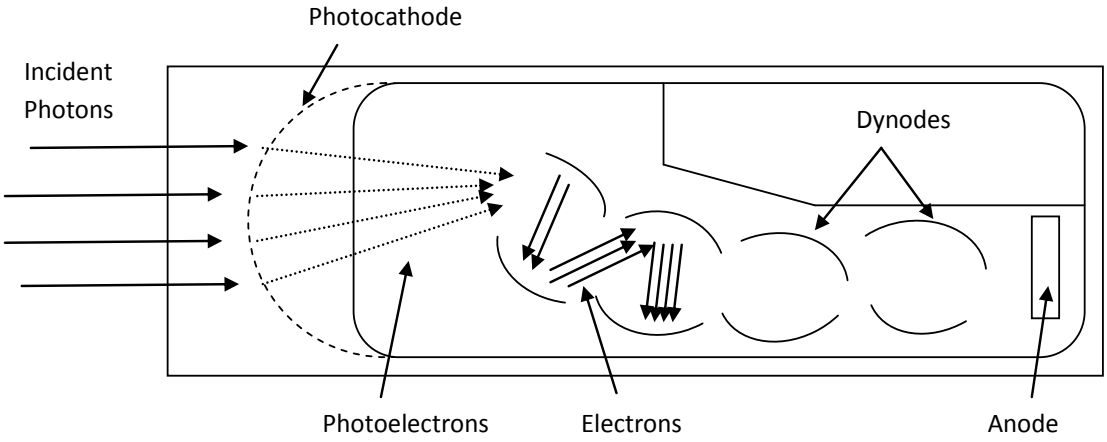

Figure 2-10: Photomultiplier tube

2.6.2 Chip and Reader Distribution

TLD chips inherently have great statistical variation, both between chips and within a given chip. It is standard practice to accept TLD chips that read within 50 percent of other chips as a 'good' measurement. To minimize inconsistent results, a TLD chip quality assurance assessment was performed. Our initial 300 TLD chips were irradiated with a 10 μCi Cs-137 button source to deliver the most uniform exposure to each of the chips for a time period of 30 seconds. The 30 second time period corresponds to delivering a dose of about 0.63 rad to the TLD chip. The TLD chips were placed in 10 mL glass beakers and labeled. The chips were then read out and the respective TLD output was recorded. The chips were annealed and the irradiation process was repeated. The chips that read within 25 percent for both irradiations were deemed "Good" chips and were therefore used in the experiment. For purposes of error propagation, the TLD chip error was assumed to be 25 percent. Figure 2-11 displays the statistical variations of the "Good" TLD chips. The standard deviation of the "Good" chips was 16.4 percent.

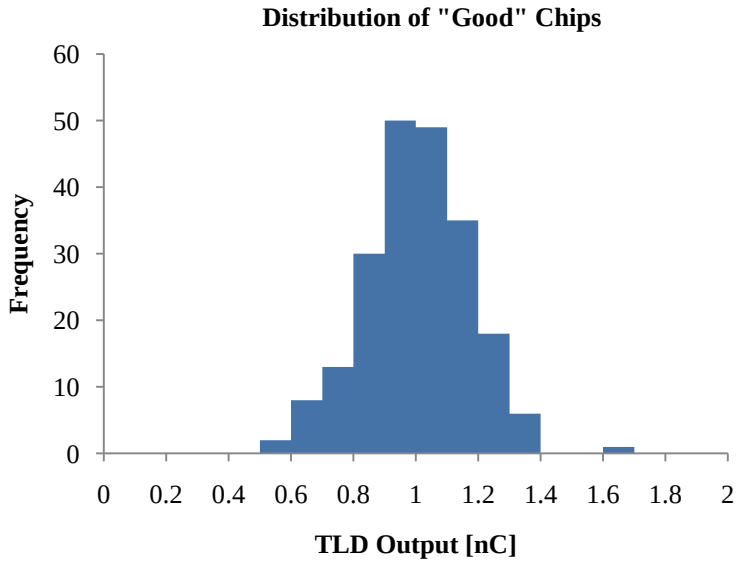

Figure 2-11: Distribution of "Good" chips

Both a Chi-Squared test and a reduced Chi-Squared test were performed on the TLD reader to determine if the counting system was reliable. A Poisson distribution around a true mean is expected if the system is responding correctly. Dark current readings, which are TLD readings with the drawer completely closed with no TLD chip placed on the planchet, were used for determining operation characteristics of the TLD reader in an effort to minimize the statistical influence of the TLD chip. The standard deviation of dark current was 4.95 percent. The reduced Chi-Squared for 39 degrees freedom was calculated to be 0.98. This value is very close to unity (p-value of 0.49 at 95% confidence); therefore it is assumed the counting system is operating properly. The Chi-Squared value was obtained from Eqn. (2.19) (Knoll 2000).

$$\chi^2 \equiv \frac{1}{\bar{x}_e}\sum_{i=1}^{N}(x_i - \bar{x}_e)^2 \qquad (2.19)$$

The Chi-Squared value is 38.4 which is within the 80 percent confidence interval of 28.2 to 50.7 (NIST Chi-Squared). Figure 2-12 displays the dark current distribution for the Chi-Squared test. A total of 10 dark current readings were taken before reading each batch of TLD chips. Each group of 10 dark current readings were very consistent; however, the dark current readings varied slightly from day-to-day. To

maximize the variability estimate, the Chi-Squared test for the dark current distribution was taken from random samplings of all the dark current readings.

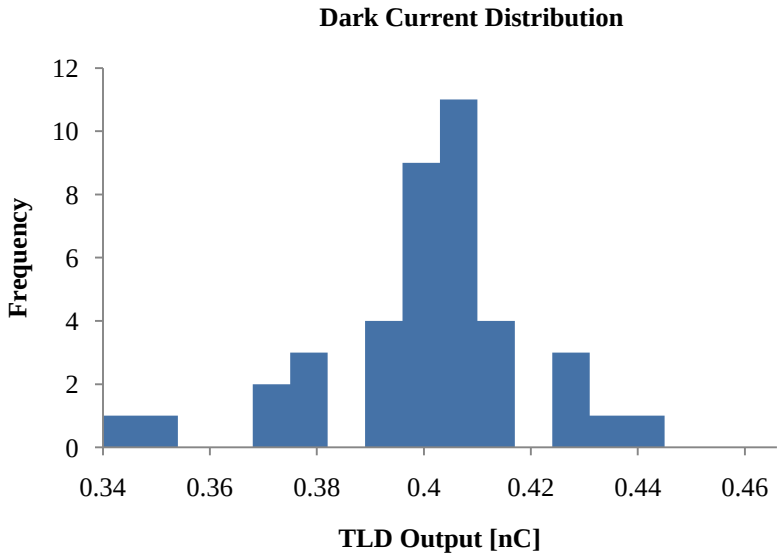

Figure 2-12: Dark current distributions

2.6.3 Limits of Detectability

To distinguish between background TLD chips and TLD chips which have been exposed, the limit of detectability must be known. The critical level L_c is the lower limit that minimizes the amount of false positives. TLD chips with values less than the critical level are assumed to have no detectable exposure data, and TLD chips with greater values than the critical level are assumed to have been exposed. Another value, $N_{D,}$ is the minimal net value that must be met to infer that real exposure data is present at 95 percent confidence. A background chip value of 0.433 nC was used to determine the critical value and the N_D value. The Eqns. (2.20) and (2.21) were used to determine the L_c and the N_D (Knoll 2000).

$$L_c = 2.326 \times \sigma_{N_B} \tag{2.20}$$

$$N_D = 4.653 \times \sigma_{N_B} + 2.706 \tag{2.21}$$

The standard deviation of the background chips was found to be 0.05 nC and the net lower limit of detection was 0.099 nC. Therefore, if the net current is greater than 0.099 nC, it is concluded that there is a readable dose signal on the chip.

2.6.3 Fade Study

To determine if fade was significantly affecting the TLD chips over the irradiation time and post irradiation time, a fade study was conducted. The C-14 and the Cs-137 sources were used for two separate fade studies to determine if fade differed between TLD chips with pure beta exposure verses a mixed beta-gamma exposure. The fade time intervals were selected based on irradiation times and post-irradiation time required to complete both the solid source and liquid source irradiations. All the solid sources had irradiation times of less than 24 hours and the liquid sources, if completed, were less than 2 weeks. Fade time intervals were 1 hr, 6 hrs, 12 hrs, 24 hrs, 48 hrs, 1 week, and 2 weeks. A total of 5 TLD chips were used for each source at each fade time interval. The TLD chips were initially irradiated for 5 minutes with either the Cs-137 or the C-14 source and were stored in darkness during the fade period. Table 2-2 provides TLD chip data for both the Cs-137 and C-14 sources.

Table 2-2: Fade study data

C-14	1 hr	6 hr	12 hr	24 hr	48 hr	1 week	2 week
Mean	13.15	13.22	13.14	11.18	13.50	12.33	11.04
STD (σ)	3.65	3.50	2.17	2.70	1.05	2.02	2.72
Mean - σ	9.50	9.72	10.97	8.47	12.45	10.31	8.32
Mean + σ	16.80	16.73	15.31	13.88	14.55	14.36	13.76
Cs-137	**1 hr**	**6 hr**	**12 hr**	**24 hr**	**48 hr**	**1 week**	**2 week**
Mean	6.11	5.33	6.02	6.98	7.06	5.53	5.28
STD (σ)	1.57	1.29	2.53	2.74	1.13	1.03	1.13
Mean - σ	4.54	4.04	3.50	4.24	5.93	4.51	4.15
Mean + σ	7.68	6.62	8.55	9.72	8.19	6.56	6.41

The means of the time intervals at 2 weeks were within the range of the mean plus or minus the standard deviation for the initial 1 hour time period. This indicates that fade is not a significant factor for fade times of less than 2 weeks. A fade factor for

increased accuracy was found by using an exponential fit. Figures 2-13 and 2-14 display the fade study and the exponential fit found via Matlab for the Cs-137 study and the C-14 study, respectively.

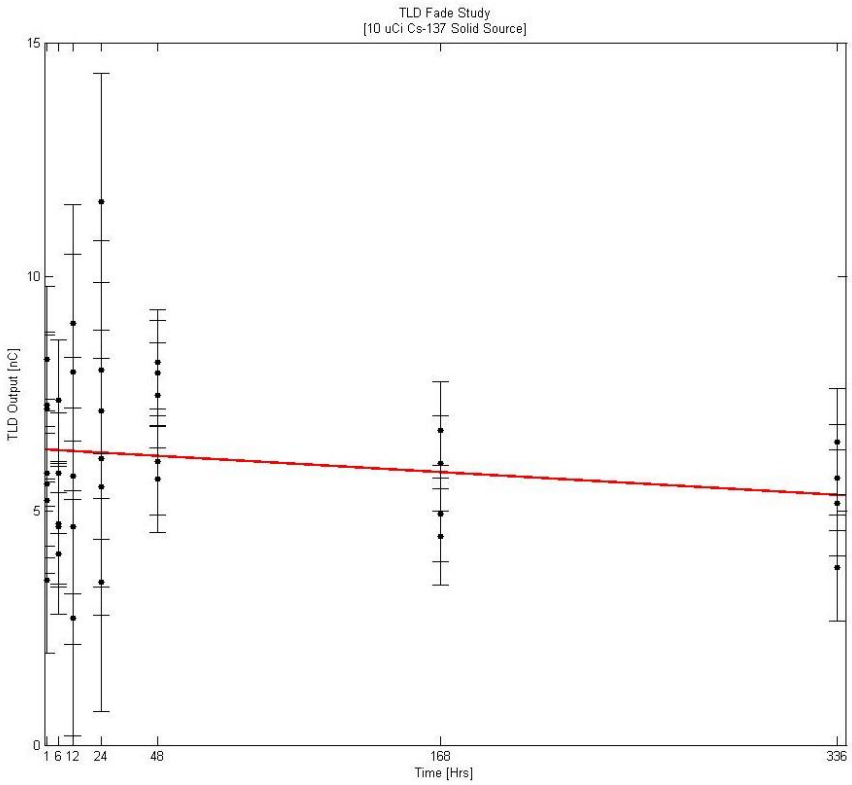

Figure 2-13: Cs-137 fade study

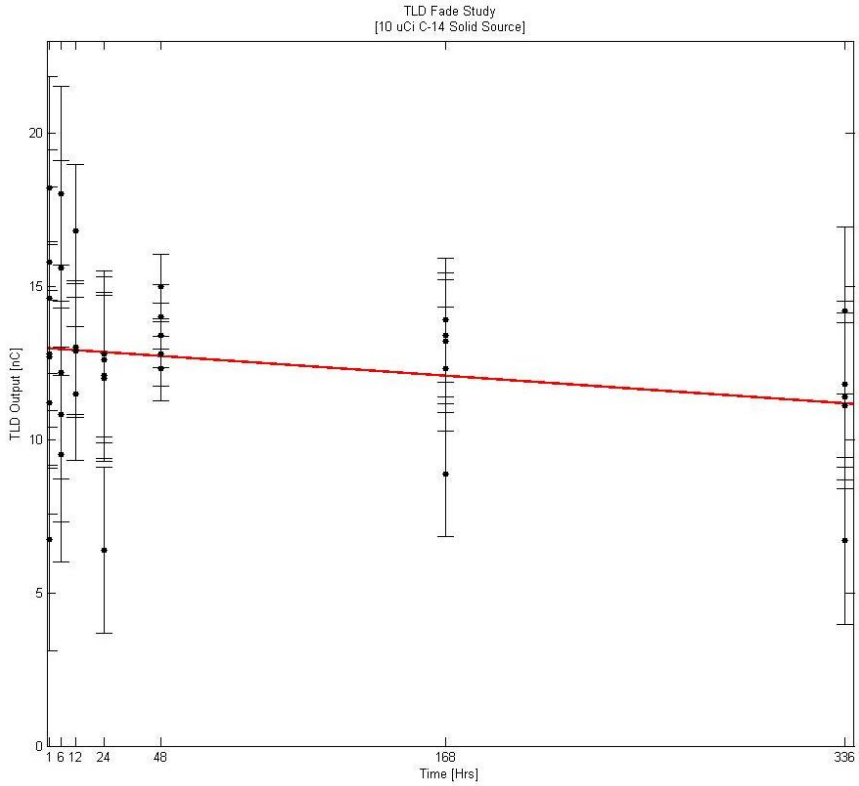

Figure 2-14: C-14 fade study

A fade factor was developed from the exponential fits via normalizing the factor with mean value at time 1 hour. Figure 2-15 displays the two fade factors. The red line represents the C-14 source and the blue line represents the Cs-137 source.

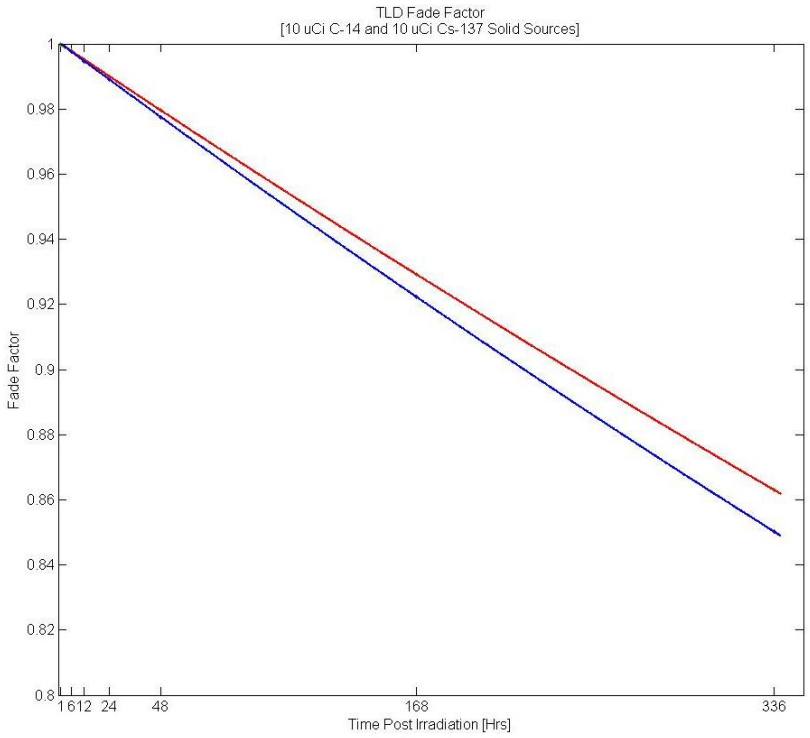

Figure 2-15: Fade factor

Based on the fade study, there is not a significant difference of fade between pure beta exposure and mixed beta-gamma exposure. This fade study was conducted only for fade times up to 2 weeks. If greater fade time is applicable then a longer fade study is required. All the experiments were irradiated for less than 24 hours and the time between irradiation and processing was less than 24 hours. The TLD chips in the experiments for this research have a fade factor of greater than 0.98; therefore, approximately 2 percent of the signal was lost due to fade. The fade factor of 2 percent was deemed insignificant and fade correction was not applied to the final experimental results.

A single-factor ANOVA statistical test was applied to the collected fade data for the 7 time intervals. The null hypothesis for the ANOVA test states that the mean for each time interval is statistically equivalent. The C-14 F_{obs} (0.71) is less than F_{crit} (2.42); therefore, the null hypothesis is not rejected. The Cs-137 F_{obs} (0.81) is less than F_{crit} (2.43); therefore, the null hypothesis is not rejected. Based on the ANOVA

test, the mean for the time interval is statistically equivalent; therefore, fade is not a concern over the 48 hour period.

2.6.4 Fluorescent Light Study

To determine if ultraviolet light from fluorescent lights affects the TLD chips, a literature review was conducted along with a fluorescent light study. TLD exposure to visible or ultraviolet light can cause false photon emissions upon processing. If an irradiated TLD is exposed to visible or ultraviolet light, the chip may lose or redistribute electrons within its structure (Gad 1991). An IAEA study was performed by Regulla, et al (1979) concerning visible light exposure to different TLDs. The visible light exposure study for LiF TLD-100s showed no significant difference between chips exposed to visible light for 1 hour to those stored in darkness. There is no data for LiF TLD-100s exposed in excess of 1 hour.

Daylight is not a concern for this experiment since all the lighting in the laboratory is of fluorescent light. Fluorescent lights use electricity to excite mercury vapor and the excited mercury atoms produce ultraviolet light which then interacts with a phosphor to fluoresce in the visible spectrum. The literature review did not find a UV light study based solely on exposure to fluorescent lights; therefore, a fluorescent light study was conducted.

The C-14 and the Cs-137 source were used for two separate light studies to determine if fluorescent light had a different effect on TLD chips with a pure beta exposure verses a mixed beta-gamma source. The exposure time intervals were selected based on the most common irradiation time periods of 1, 2, 3, 6, 12, and 24 hours. A total of 5 chips were irradiated for 5 minutes with each source. The chips were then exposed to fluorescent light for the desired time increment and processed. Figures 2-16 and 2-17 display the results of the fluorescent light study for the Cs-137 source and the C-14 source, respectively. Table 2-3 displays the average and the standard deviation of the 5 chips at each time interval.

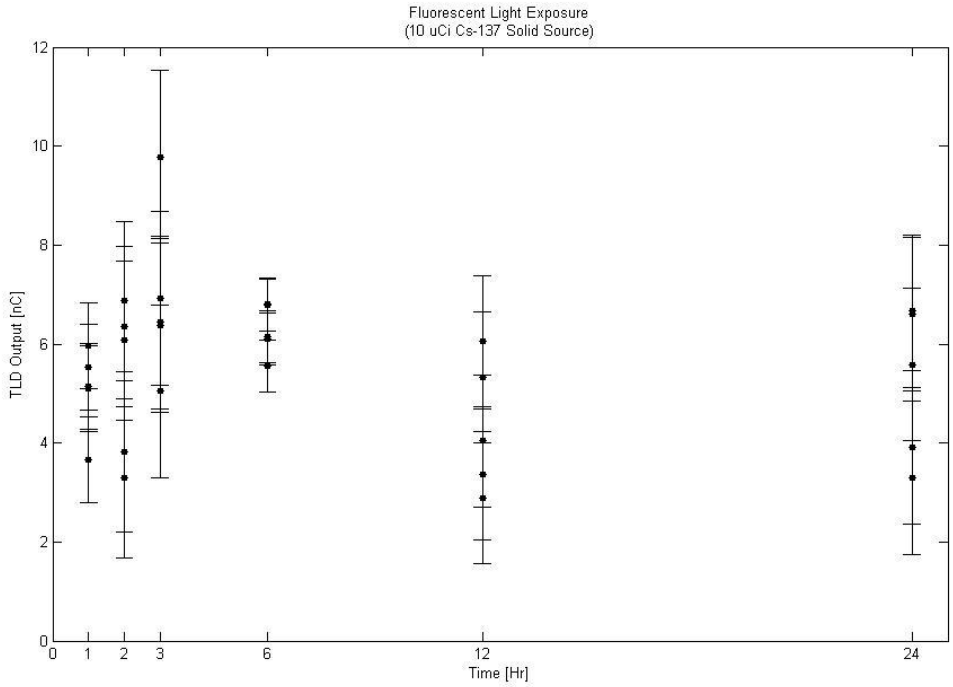

Figure 2-16: Cs-137 fluorescent light exposure

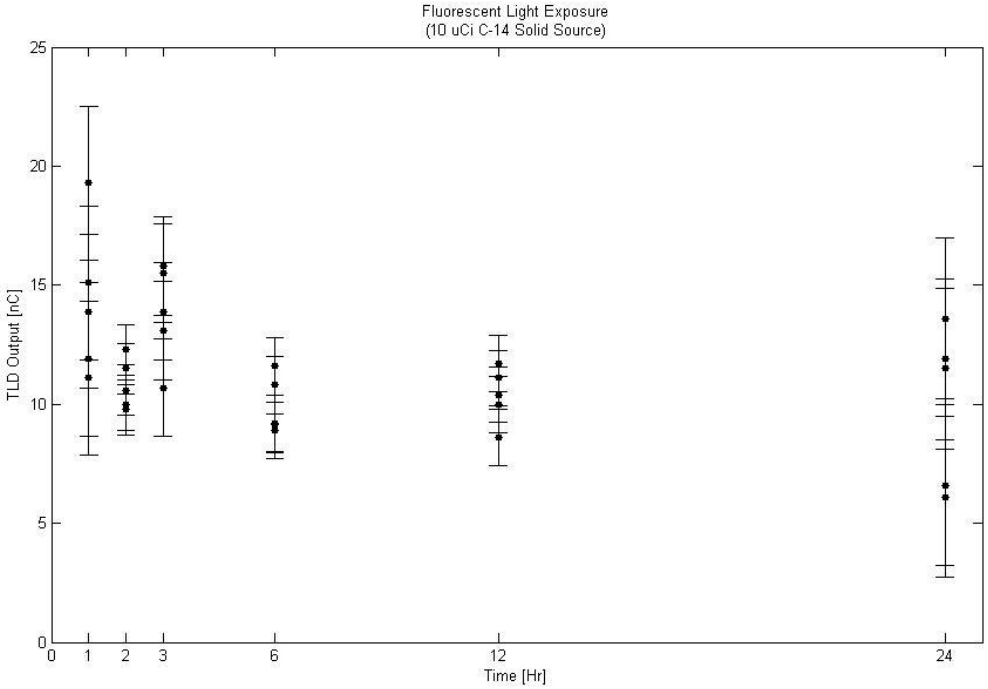

Figure 2-17: C-14 fluorescent light exposure

Table 2-3: Fluorescent light results

C-14	No Light 1 hr	1 hr	2 hr	3 hr	6 hr	12 hr	24 hr
Mean	14.22	14.26	10.83	13.80	9.93	10.36	9.94
STD (σ)	2.53	3.23	1.06	2.06	1.20	1.18	3.38
Mean - σ	11.69	11.03	9.77	11.74	8.74	9.18	6.56
Mean + σ	16.74	17.49	11.89	15.86	11.13	11.54	13.32
Cs-137	**No Light 1 hr**	**1 hr**	**2 hr**	**3 hr**	**6 hr**	**12 hr**	**24 hr**
Mean	6.55	5.08	5.28	6.91	6.28	4.34	5.21
STD (σ)	1.18	0.87	1.61	1.75	0.53	1.33	1.55
Mean - σ	5.37	4.22	3.67	5.16	5.75	3.01	3.67
Mean + σ	7.73	5.95	6.89	8.66	6.80	5.67	6.76

The 24 hour result is within the no-light standard's mean plus or minus one standard deviation for both the C-14 and the Cs-137; therefore, fluorescent light exposure is assumed to not affect the irradiated TLD chips. This is expected since the LiF TLD-100s are reported to have very low sensitivity to ultraviolet light.

All experiments were performed to minimize potential effects of fluorescent light exposure as much as possible. TLD chip trays were covered with tin foil when transporting chips between labs and when storing them. It is estimated that the TLD chips received less than 1 hour of direct exposure to fluorescent lights. During the experiments, dark paper was placed over the setup to prevent ultraviolet exposure from beneath the chip; the source itself is opaque to visible light.

A single-factor ANOVA statistical test was applied to the collected fluorescent light data for the 6 time intervals. The null hypothesis for the ANOVA test states that the mean for each time interval is statistically equivalent. The C-14 F_{obs} (4.25) is greater than F_{crit} (2.43); therefore, the null hypothesis is rejected. The Cs-137 F_{obs} (2.54) is greater than F_{crit} (2.43); therefore, the null hypothesis is rejected. Based on the ANOVA test, the mean for the time interval is not statistically equivalent; indicating fluorescent light is a concern with exposures for long durations.

A second ANOVA test was performed using just the standard no light exposure data and the 1 hour exposure data. The C-14 F_{obs} (0.0006) is less than F_{crit} (5.11); therefore, the null hypothesis is not rejected. The Cs-137 F_{obs} (5.28) is greater than F_{crit} (5.12); therefore, the null hypothesis is rejected. Based on the ANOVA test the fluorescent light is affecting the Cs-137 exposed chips but not the C-14. This can be attributed to the variance in TLD chips – more chips would increase statistical accuracy. No fluorescent light correction was applied to the TLD chips due to the limited time the TLDs were exposed to the fluorescent light.

2.7 Radiochromic Film

Radiochromic film responds by direct coloration of a material via polymerization induced by ionizing radiation. Radiochromic film has many advantages over radiographic film. Radiographic film is sensitive to room light and requires wet chemical processing, while radiochromic films are insensitive to visible light and are self processing (Niroomand-Rad 1998). There are three basic reactions required for radiation induced polymerization: (1) initiation by ionizing radiation; (2) propagation; and (3) termination. The radiation provides radicals or ions in the initiation step. The radicals react with nearby monomers, thus adding 10^4 to 10^5 monomer units to the polymer chain (Charlesby 1965). The addition of monomers to the chain is known as the propagation stage. Termination is the end of the polymer chain and can be initiated by a reaction with another radical. The conversion from monomer to polymer in radiochromic film is measured by a blue coloration of the film: the film is otherwise clear.

Gafchromic EBT dosimetry film is produced by International Specialty Products primarily for quality assurance applications for radiotherapy. The Gafchromic film is near tissue equivalent. Table 2-4 provides the approximate atomic composition percentages (International Specialty Products). Two types of Gafchromic EBT dosimetry film were used in this research - a standard thickness film and a thin film.

Table 2-4: Atomic composition of Gafchromic Film

Layer Material	Element	Composition [Atom %]
Polyester Base	Carbon	45
	Hydrogen	36
	Oxygen	19
Sensitive Layer	Carbon	31
	Nitrogen	56
	Hydrogen	5
	Oxygen	8
Adhesive Layer	Carbon	33
	Hydrogen	50
	Oxygen	17

The standard film is composed of 5 layers, while the thin film is composed of only 4 layers. The thin film is missing one of the polyester outer layers, thus the active layer is exposed. Both films are composed of 3 different material types. Figure 2-18 is a diagram of the Gafchromic film layer composition along with the thickness of each layer. The Gafchromic film Z_{eff} ranges from 6.0 to 6.5. The Gafchromic film has a useful range of 10^{-2} to 10^{6} Gy.

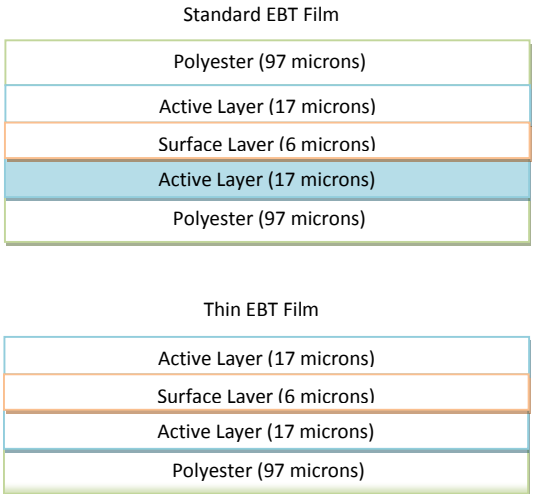

Figure 2-18: Diagram of Gafchromic film layer composition

2.8 Monte Carlo N-Particle (MCNP) Computational Code

A *F8 tally was used to obtain the energy deposited in a cell or defined volume in MCNP. The *F8 tally has the unit of MeV per incident radiation particle. The tally essentially tracks the energy of the particle entering the cell and the energy of the

particle when it leaves the cell, thus the MeV deposited per particle in that cell is the output. Every *F8 tally must designate the energy bin range over which to bin a response. The energy bin should include a zero energy bin to eliminate the negative energy pulse heights caused by knock-on electrons (MCNP5 Manual Vol. II). The energy bin must be large enough to include the largest possible energy for a given scenario.

MCNP default cross sections for energy loss rate, energy straggling, multiple scattering, knock-on electrons, and bremsstrahlung are calculated based on a fixed energy grid (Reynaert 2002). The default MCNP collisional energy loss is referred to as a class one code. The main disadvantage of this is the loss of conservation of energy and momentum for the particle interactions. The secondary particles do not affect the direction or the energy of the primary particles. Another disadvantage is that the electron sub-step needs to be interpolated since it will not equal one of the fixed grid energies. This new interpolated energy is applied to the secondary particle; however, it is not applied to determining multiple scattering angles. All MCNP runs in this research used the DBCN 17j 2 card.

3.0 MCNP Models

There are two main MCNP scenarios that were modeled – exposure from a liquid source and from a solid source. Radioactive sources of ^{14}C, ^{137}Cs, ^{133}Ba, ^{60}Co, and $^{90}Sr/^{90}Y$ were modeled. In the simulation, polyethylene was placed between the source and the TLD to achieve the desired depths of 7 mg/cm^2, 30 mg/cm^2, 50 mg/cm^2, 100 mg/cm^2, 300 mg/cm^2, and 1000 mg/cm^2. The TLD chip was placed on a layer of Plexiglas to minimize backscatter into the TLD chip.

There are two liquid models due to two different liquid source amounts. A 5 µL drop was used to approximate a point source. The drop was modeled as a hemisphere with a diameter of approximately 2.6 mm. The second drop model was used to approximate an infinite source; therefore a 10 µL drop was used. The 10 µL drop was approximated as an ellipsoid due to the loss of surface tension as the volume of water is increased. The 10 µL drop was modeled with a 4 mm diameter. The diameters of the liquid drops were determined both mathematically and from actual measurement. The equation used to approximate the diameter for the hemisphere of a 5 µL drop is provided in Eqn. (3.1).

$$\frac{\frac{4}{3}\pi R^3}{2} = 0.005\ ml \tag{3.1}$$

The 10 µL drop was measured to obtain a diameter. The radius parameter in the ellipsoid MCNP geometry was set to the measured radius and the "height" of the ellipsoid was modified to achieve a 10 mm^3 volume, i.e., equivalent to 10 µL.

3.1 Solid Encapsulation Source Model

3.1.1 Button Source Encapsulation

The Ba-133, Co-60 and Cs-137 are button configuration sources. The encapsulation material is Plexiglas with a radius of 1.25 cm. The source itself is located on a 2.5 mm diameter disk with a thickness of 50 µm. The source is located 0.38 mm from the bottom of the encapsulation. Figure 3-1 is a diagram of the solid

source model. Cell 100 in the MCNP simulation is the source encapsulation, cell 200 is the polyethylene (which will vary in thickness to achieve the desired TLD depths), and cell 300 is the TLD chip. The dimensions of the TLD chip are 0.3175 cm x 0.3175 cm x 0.01524 cm. Cell 400 is Plexiglas and cell 500 is air.

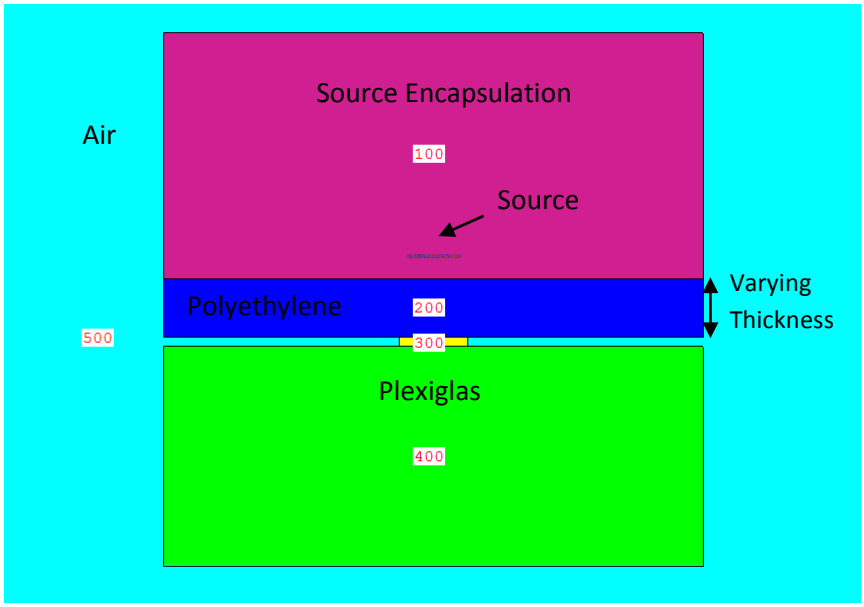

Figure 3-1: Solid source configuration for Ba-133, Co-60, and Cs-137

3.1.2 Laminate Source Encapsulation

The C-14 source is a laminate source. The encapsulation material is polyethylene with a radius of 1.902 cm and the source itself is a 2.5 mm diameter disk with a thickness of 25 μm. The source disk is located 0.127 mm from the bottom of the encapsulation. Figure 3-2 is a diagram of the solid C-14 source model.

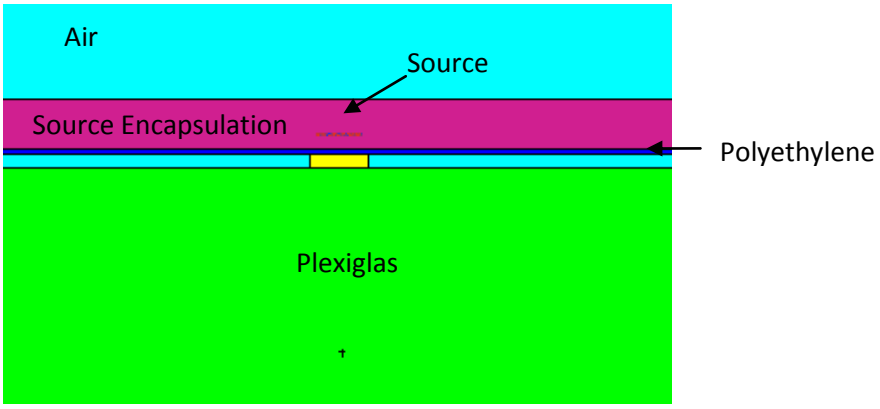

Figure 3-2: Diagram of laminate C-14 source

3.1.2 Foil Source

The Sr-90/Y-90 source is dried on a thin foil. The dimensions of the foil source were approximated since no data from the manufacturer could be obtained. The foil source encapsulation was assumed to be composed of the metal tin, while the source itself was defined as strontium metal. The radius of the source was measured to be 1.11 cm and the thickness was approximated as 50 µm. There is no source encapsulation window. Figure 3-3 is a diagram of the Sr-90 foil source.

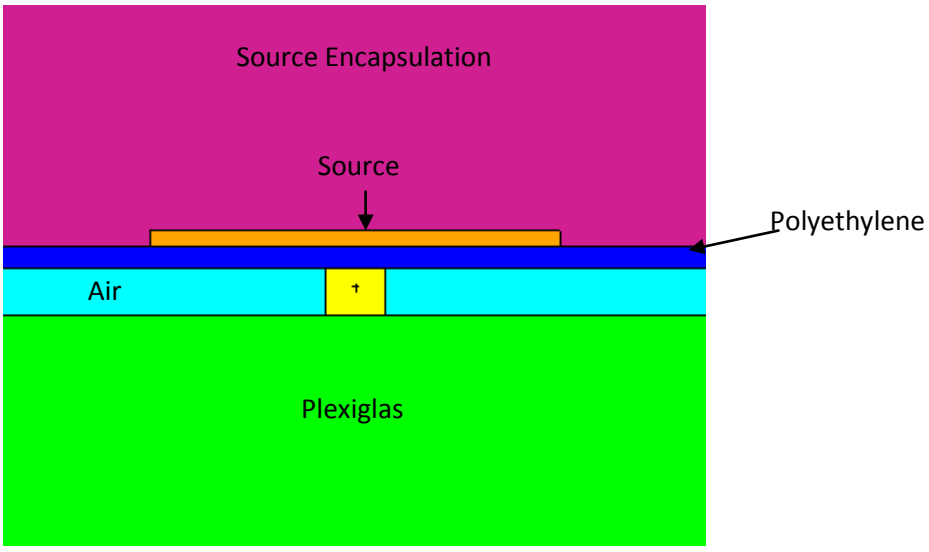

Figure 3-3: Sr-90 Foil source

3.2 Liquid Source Model

The liquid water droplets were modeled with a uniform source distribution within the droplet. A layer of cellophane was placed between the source and the polyethylene to prevent contamination of the polyethylene and TLD chips. The cellophane has an approximate thickness of 0.00127 cm or 1 mg/cm^2. Figure 3-4 provides a diagram of the 5 µL source droplet and Figure 3-5 provides a diagram of the 10 µL source droplet.

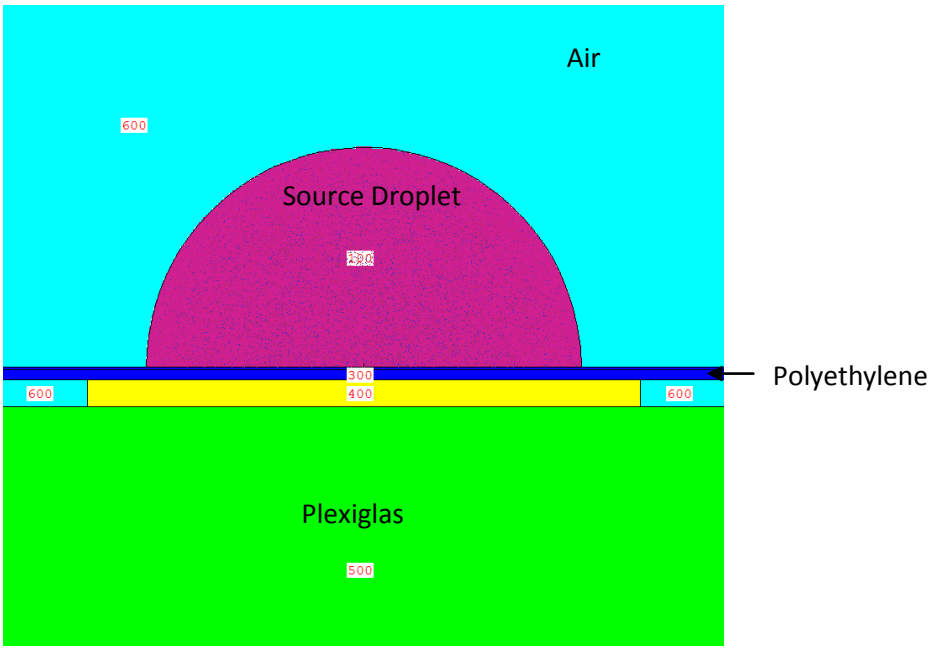

Figure 3-4: A 5 µL liquid source drop

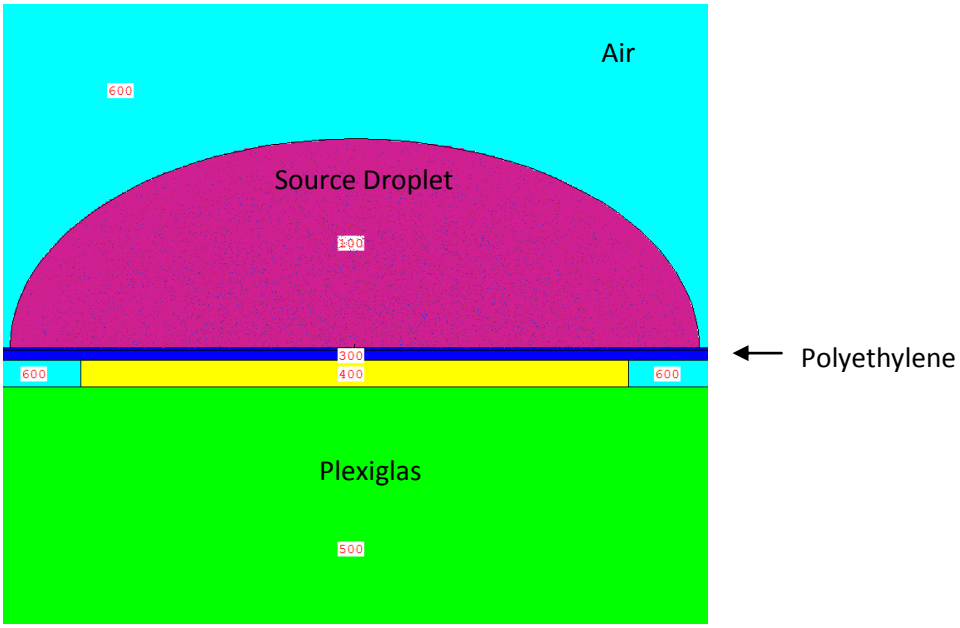

Figure 3-5: A 10 µL liquid source drop

3.3 MCNP Material Parameters

The materials used in modeling the source configurations are provided in Table 3-1. The negative values indicate a weight fraction, whereas the positive values indicate an atomic fraction.

Table 3-1: Materials used in MCNP modeling

Material	MCNP ZAID Input	
Air	7000	-0.789
	8000	-0.201
	18000	-0.01
LiF	3000	1
	9000	1
Plexiglas	1000	-0.0805
	6000	-0.5998
	8000	-0.3196
Polyethylene	6000	2
	1000	4
Strontium	38000	1
Tin	50000	1
Water	1000	2
	8000	1

3.4 TLD Chip Integration Modifier

The output from the TLD reader is for the entire chip; therefore, it is impossible to determine the percentage of dose deposited in only a fraction of the chip. The TLD chip is the thinnest manufactured chip at this time, but the chip itself is still 40 mg/cm^2. The thickness required for dose reporting is 1 mg/cm^2. This density thickness corresponds to 10 μm of tissue, which is approximately the thickness of a cell. To determine the contribution of total dose that is distributed in the first 1 mg/cm^2 of the chip, a chip integration modifier was developed.

To determine the dose distribution profile of the TLD chips, multiple MCNP tallies were superimposed on the TLD chips for each source scenario and depth configuration. A total of fifty *F8 tallies of 3 μm each were used to track dose deposition varying in the thickness of the TLD chip. The results of the fifty tallies were plotted in Matlab with respect to the depth within the TLD chip, and then an exponential fit was determined. Figure 3-6 displays an MCNP5 simulation input of the fifty tallies used to integrate dose through the TLD chip.

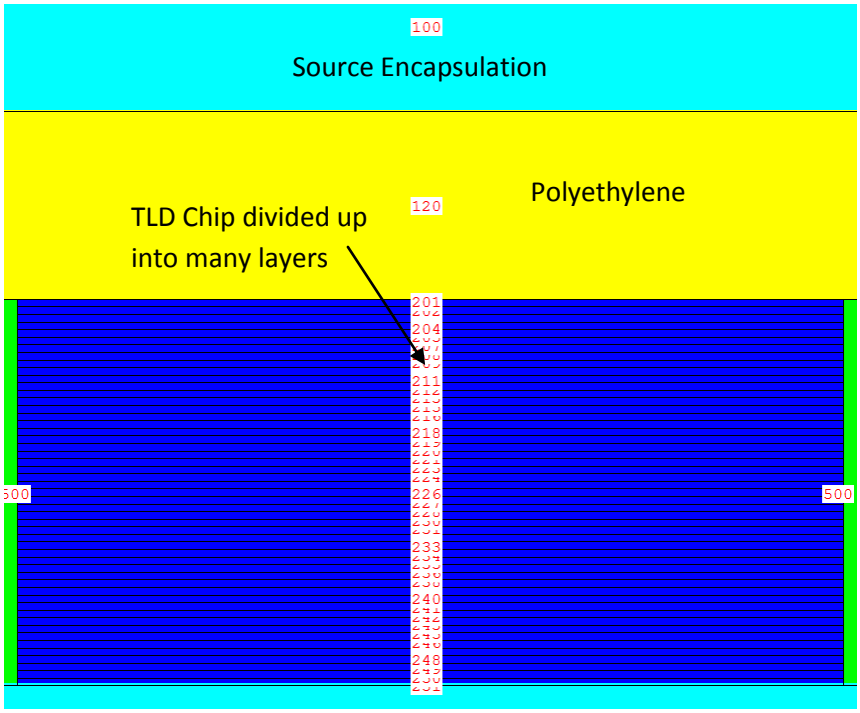

Figure 3-6: MCNP TLD chip integration model

The thickness of the TLD chip that would be equivalent to the 1 mg/cm^2 is approximately 3.79 µm. The exponential fits for TLD chips were integrated from 0 to 3.79 µm and from 0 to the entire thickness of 152 µm. A percentage of deposited dose was then found for the first 3.79 µm of the TLD chips. These percentages can be applied to the TLD outputs for an approximate dose for the first 1 mg/cm^2 of the TLD chip. Tables 3-2 to 3-6 provide the exponential fits, integration values, and percentage of dose deposited in the first 3.79 µm of the TLD chip. The coefficients A and B for the chip integration results pertain to Eqn. (3.2).

$$Y = Ae^{Bx} \tag{3.2}$$

Table 3-2: Cs-137 TLD chip integration results

Density Thickness [mg/cm^2]	A	B	R^2	Integrated 3.79 µm	Total Chip 152 µm	Percent in 3.79 µm
0	4.82E-04	-6.98E-03	0.99	1.80E-02	4.51E-02	3.98
7	3.84E-04	-6.69E-03	0.99	1.44E-03	3.66E-02	3.92
30	1.92E-04	-5.63E-03	0.99	7.20E-04	1.96E-02	3.67
50	1.14E-04	-4.73E-03	0.99	4.29E-04	1.24E-02	3.46
100	4.32E-05	-5.67E-03	0.99	1.62E-04	4.40E-03	3.67
300	9.03E-05	-1.71E-03	0.90	3.41E-06	1.21E-04	2.82
1000	8.24E-08	-1.42E-03	0.33	3.11E-07	1.13E-05	2.76

Table 3-3: Co-60 TLD chip integration

Density Thickness [mg/cm^2]	A	B	R^2	Integrated 3.79 µm	Total Chip 152 µm	Percent in 3.79 µm
0	6.45E-05	-1.43E-02	0.99	2.38E-04	3.99E-04	5.95
7	3.58E-05	-1.17E-02	0.98	1.33E-04	2.54E-03	5.21
30	8.18E-06	-2.58E-03	0.88	3.10E-05	1.03E-03	2.99
50	5.97E-06	-9.85E-04	0.87	2.30E-05	8.43E-04	2.67
100	4.29E-06	-8.43E-04	0.81	1.62E-05	6.12E-04	2.65
300	1.47E-06	-9.83E-04	0.81	5.56E-06	2.08E-04	2.67
1000	1.74E-07	-1.94E-03	0.48	6.56E-07	2.29E-05	2.86

Table 3-4: Ba-133 TLD chip integration

Density Thickness [mg/cm^2]	A	B	R^2	Integrated 3.79 µm	Total Chip 152 µm	Percent in 3.79 µm
0	4.16E-06	-1.68E-03	0.95	1.57E-05	5.58E-04	2.81
7	3.72E-06	-1.63E-03	0.96	1.40E-05	5.01E-04	2.80
30	2.67E-06	-1.37E-03	0.91	1.01E-05	3.66E-04	2.75
50	2.08E-06	-1.21E-03	0.86	7.87E-06	2.89E-04	2.72
100	1.27E-06	-1.05E-03	0.81	4.78E-06	1.78E-04	2.69
300	3.18E-07	-3.85E-04	0.28	1.20E-06	4.70E-05	2.56
1000	3.74E-08	-6.79E-04	0.01	1.42E-07	5.41E-06	2.61

Table 3-5: Sr-90 TLD chip integration

Density Thickness [mg/cm^2]	A	B	R^2	Integrated 3.79 µm	Total Chip 152 µm	Percent in 3.79 µm
0	1.52E-04	-4.77E-03	0.95	5.71E-04	1.64E-02	3.47
7	1.20E-04	-4.08E-03	0.97	4.51E-04	1.36E-02	3.32
30	7.65E-05	-3.14E-03	0.97	2.88E-04	9.47E-03	3.04
50	5.74E-05	-2.54E-03	0.97	2.17E-04	7.24E-03	3.00
100	3.47E-05	-1.59E-03	0.93	1.31E-04	4.69E-03	2.80
300	1.01E-05	-1.82E-03	0.84	3.80E-05	1.34E-03	2.83

Table 3-6: C-14 TLD chip integration

Density Thickness [mg/cm^2]	A	B	R^2	Integrated 3.79 µm	Total Chip 152 µm	Percent in 3.79 µm
0	3.10E-05	-1.25E-01	0.99	9.35E-05	2.48E-04	37.73
7	1.11E-06	-1.89E-01	0.98	3.01E-06	5.90E-06	51.08

The R^2 value measures how well the exponential fit describes data points. The R^2 decreases as the density thickness is increased. This decrease is attributed to two possible sources. First, at the greater density thicknesses of 300 and 1000 mg/cm^2 the main dose contribution is from gamma rays. The gamma ray deposits energy in a relatively even and linear distribution as it passes through the TLD chip, unlike the beta particles which have an exponential energy deposition. The R^2 value is lower at greater depths due to the type of regression fit used. An exponential fit was used; however, a linear fit for the gamma ray contributions would yield a more accurate R^2 value. Second, at greater depths there are fewer particles at lower energies that are depositing energy- this affects the MCNP tallies. The smaller an MCNP tally amount, the greater variability there is in the result. The 3 µm thick tallies require at least 10^8 particles to be simulated in order to obtain relative errors less than 5 percent; however, there is still variability between the 3 µm thick tallies despite every tally passing the

statistical checks. A solution would be to simulate more particles, on the order of 10^9; however, this will dramatically increase computational run time to over a week, depending upon the available computing power.

The *F8 tally (energy deposited per particle) over the thickness of the TLD chip for each density thickness is provided in Figures 3-7 to 3-14. The beta particles deposit energy in an exponential matter, whereas the gamma ray energy deposition has more of a linear fit than exponential for the TLD chip thickness.

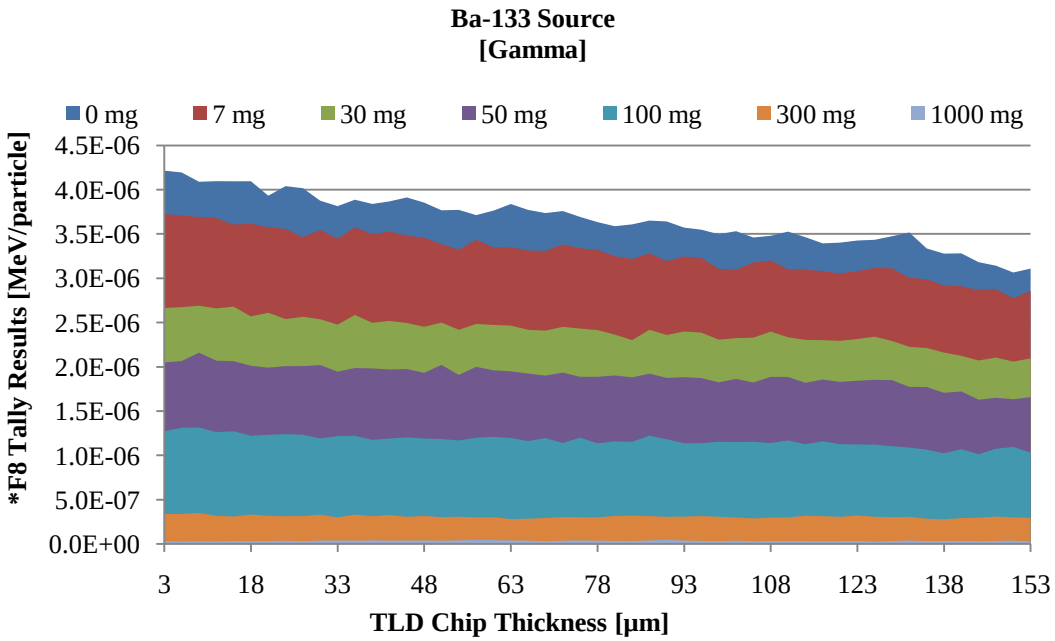

Figure 3-7: Ba-133 energy deposited through TLD chip

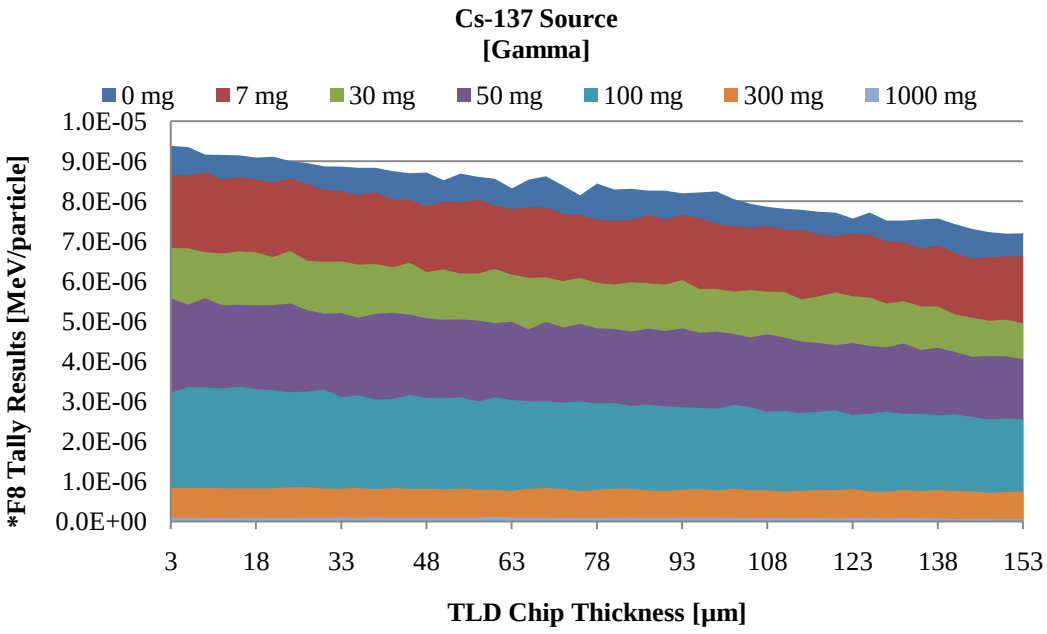

Figure 3-8: Cs-137 gamma energy deposited through TLD chip

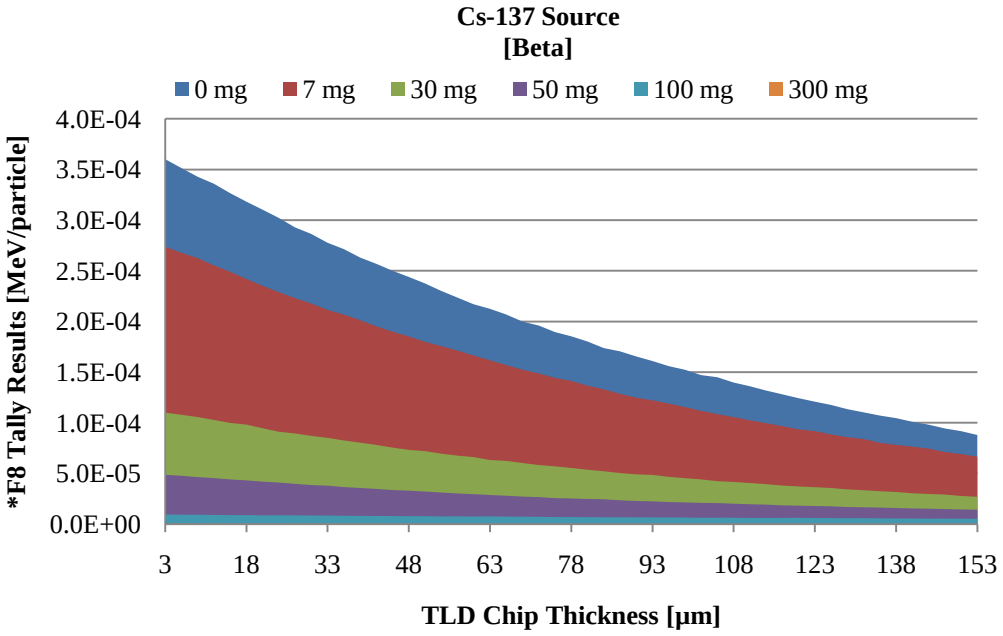

Figure 3-9: Cs-137 beta energy deposited through TLD chip

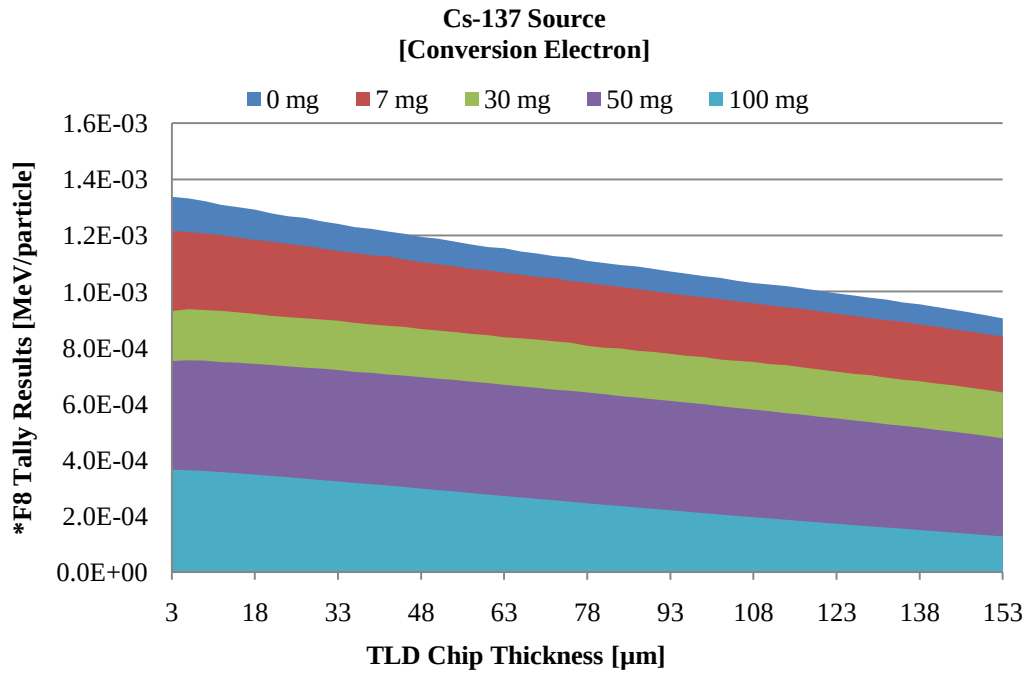

Figure 3-10: Cs-137 conversion electron energy deposited through TLD chip

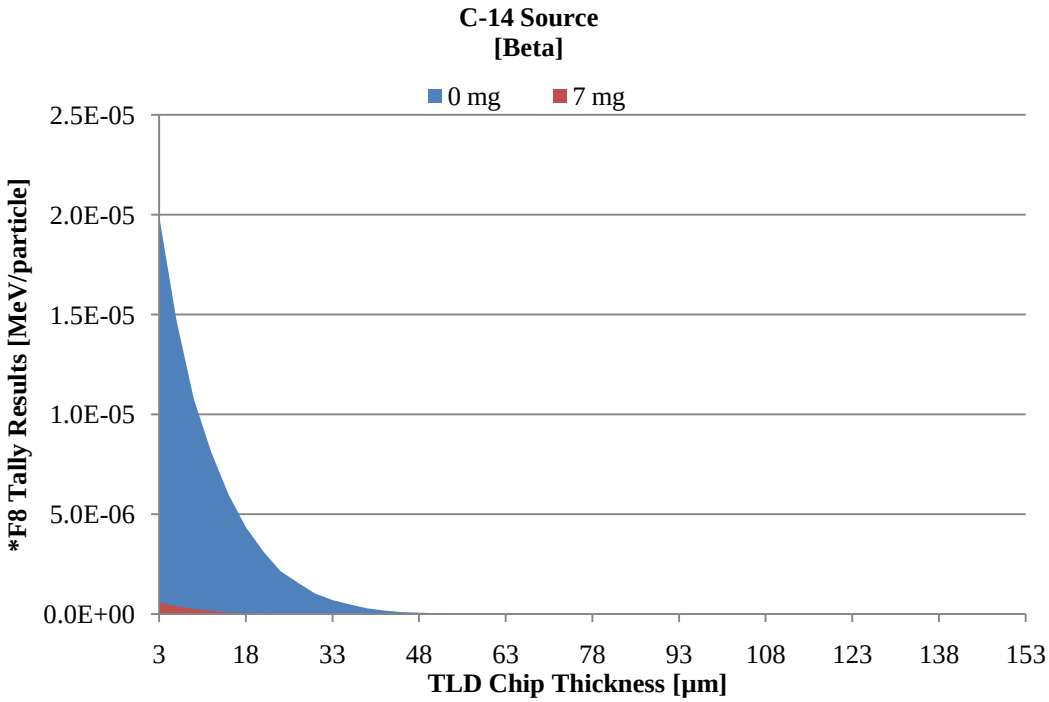

Figure 3-11: C-14 energy deposited through TLD chip

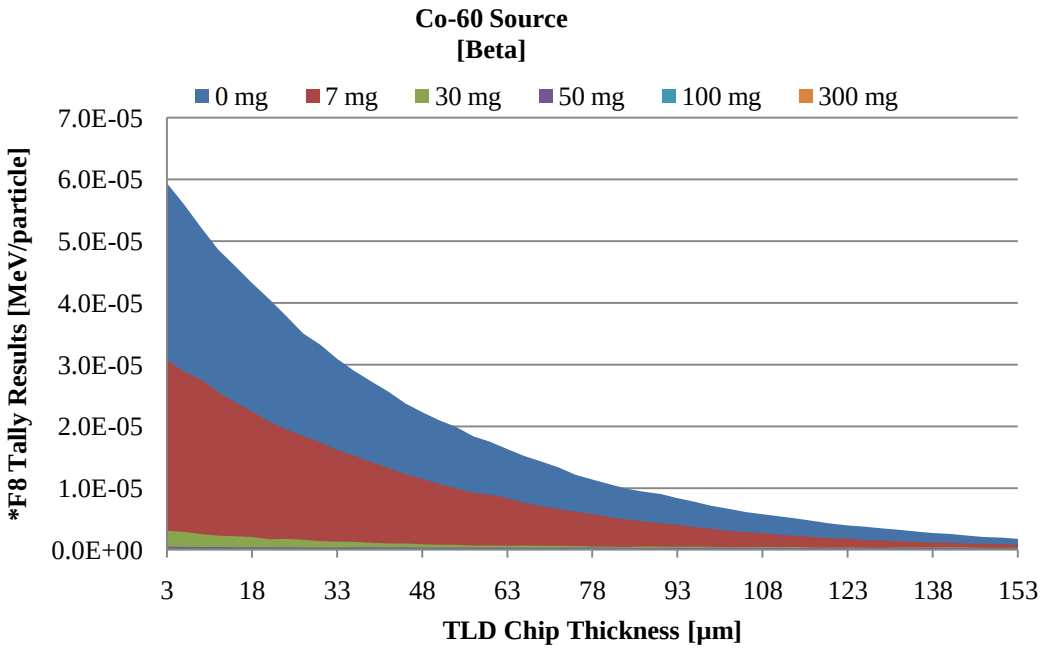

Figure 3-12: Co-60 beta energy deposited through TLD chip

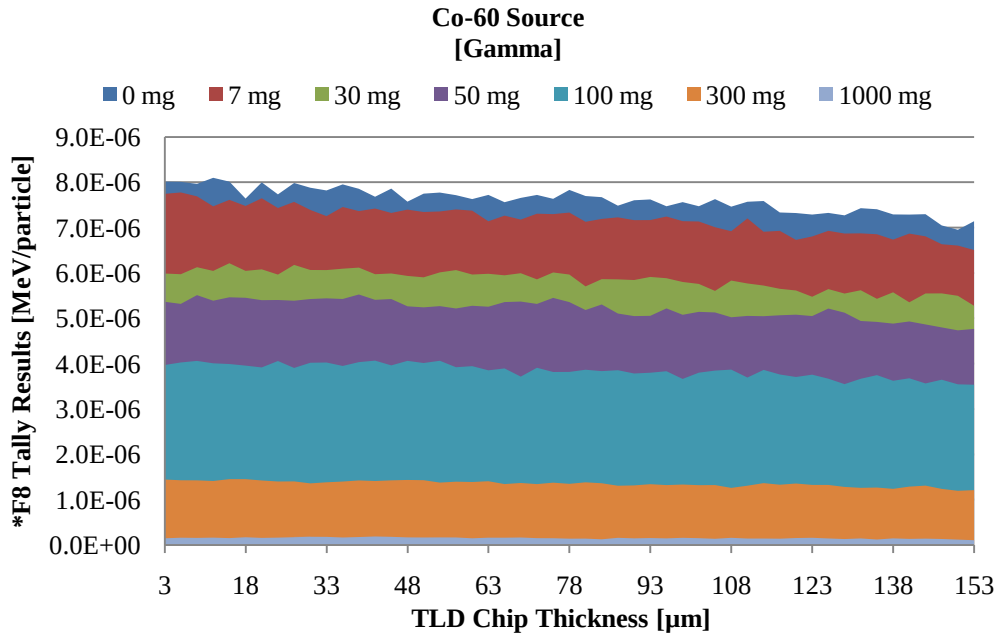

Figure 3-13: Co-60 gamma energy deposited through TLD chip

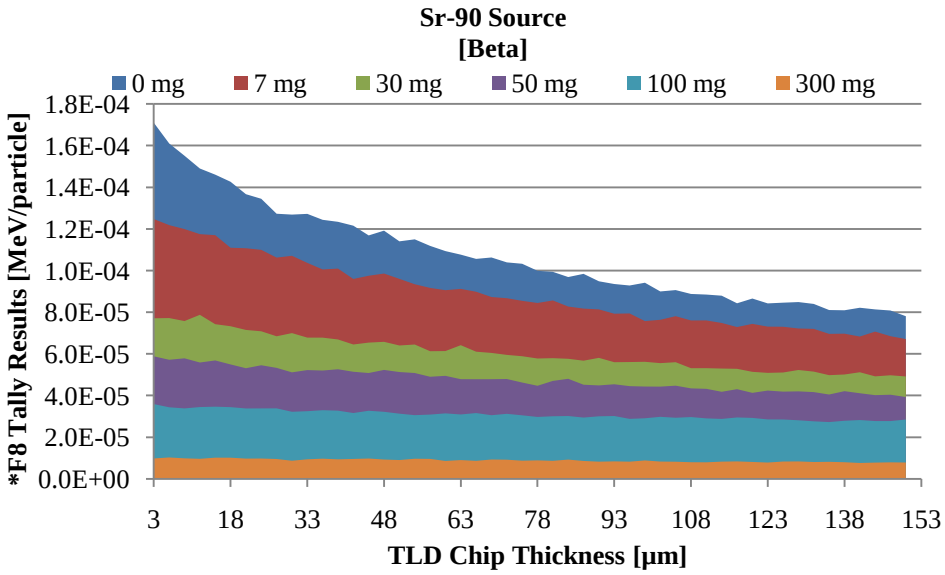

Figure 3-14: Sr-90 energy deposited through TLD chip

3.5 TLD Area Modifier

The surface area of the TLD chip which is perpendicular to the source is 0.101 cm^2. The surface area of the detector is 10 cm^2. In order to compare dose over the two averaging areas, a comparison factor must be developed. A simplified approach would be to use a factor of 100 to apply to the TLD chip area to obtain the detector area; however, MCNP simulations for each scenario yielded exact factors based on radiation type and depth in tissue. Figure 3-7 displays the MCNP5 model for the 10 cm^2 area scenario. The 10 cm^2 area is a disk with a radius of 1.784 cm.

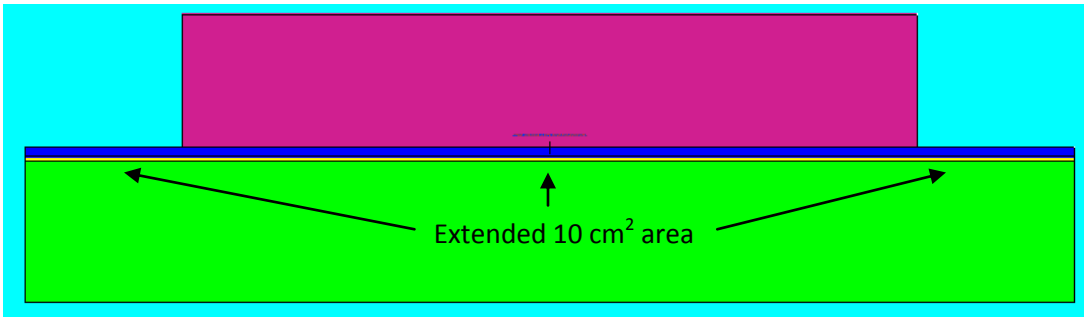

Figure 3-15: MCNP model for 10 cm^2 area

The MCNP *F8 tally results from the 10 cm^2 models were divided by the MCNP5 *F8 tally results from the TLD chip models (0.1 cm^2) to obtain an area modification factor. This factor was later applied to find the dose rate at the specified skin layer. Figures 3-7 to 3-11 are the specific area modification factors for each of the nuclides.

Table 3-7: Cs-137 area modification factors

Cs-137 [mg/cm^2]	Total for 10 cm^2	Total for 0.1 cm^2	Factor
7	1.37E-02	1.18E-02	1.16
30	8.00E-03	6.30E-03	1.27
50	5.45E-03	3.98E-03	1.37
100	2.36E-03	1.42E-03	1.66
300	4.90E-04	3.74E-05	13.11
1000	1.92E-04	3.85E-06	49.79

Table 3-8: C-14 area modification factor

C-14 [mg/cm^2]	Total for 10 cm^2	Total for 0.1 cm^2	Factor
7	7.63E-06	7.63E-06	1.00

Table 3-9: Ba-133 area modification factor

Ba-133 [mg/cm^2]	Total for 10 cm^2	Total for 0.1 cm^2	Factor
7	5.16E-04	1.66E-04	3.10
30	4.55E-04	1.20E-04	3.80
50	4.17E-04	9.22E-05	4.52
100	3.60E-04	5.61E-05	6.42
300	2.31E-04	1.46E-05	15.82
1000	9.25E-05	1.82E-06	50.87

Table 3-10: Co-60 area modification factors

Co-60 [mg/cm^2]	Total for 10 cm^2	Total for 0.1 cm^2	Factor
7	2.10E-03	7.90E-04	2.65
30	1.63E-03	3.32E-04	4.91
50	1.57E-03	2.65E-04	5.92
100	1.43E-03	1.87E-04	7.69
300	9.78E-04	6.99E-05	14.00
1000	3.85E-04	7.78E-06	49.43

Table 3-11: Sr-90/Y-90 area modification factors

Sr-90/Y-90 [mg/cm^2]	Total for 10 cm^2	Total for 0.1 cm TLD chip	Factor
7	1.64E-01	4.59E-03	35.74
30	1.14E-01	3.09E-03	36.81
50	8.93E-02	2.38E-03	37.58
100	5.83E-02	1.53E-03	38.04
300	1.68E-02	4.37E-04	38.51

3.6 MCNP Calculations

The on-contact dose rate for the solid sources, liquid sources of a 5 µL volume, and liquid sources of a 10 µL volume are displayed in Table 3-12. The on-contact configuration has the source positioned directly above and in contact with the TLD chip. To prevent contamination of the TLD chips, a cellophane barrier of density thickness 1 mg/cm^2 was modeled in MCNP for the liquid sources.

Table 3-12: On-contact dose rates determined from MCNP

Nuclide	Solid Source [rad/hr]	Liquid Source 5 µL [rad/hr]	Liquid Source 10 µL [rad/hr]
Ba-133	9.30E-01	1.00E-04	2.00E-04
C-14	3.75E-01	2.90E-03	4.40E-03
Cs-137	7.53E+01	5.70E-02	9.30E-02
Co-60	8.10E-01	3.90E-03	6.10E-03
Sr-90/Y-90	3.31E-02	1.60E-03	2.60E-04

Table 3-13: Solid source dose rates at various layers [rad/hr]

Density Thickness	Ba-133	C-14	Sr-90	Co-60			Cs-137			
[mg/cm^2]	Gamma	Beta	Beta	Beta	Gamma	Total	Beta	Gamma	CE	Total
7	8.46E-01	4.01E-02	2.77E-02	2.25E-01	3.29E-01	5.54E-01	3.91E+01	1.67E+00	2.05E+01	6.13E+01
30	6.09E-01	0.00E+00	1.86E-02	2.21E-02	2.83E-01	3.05E-01	1.56E+01	1.31E+00	1.59E+01	3.28E+01
50	4.70E-01	0.00E+00	1.43E-02	8.21E-03	2.45E-01	2.53E-01	7.11E+00	1.05E+00	1.25E+01	2.07E+01
100	2.86E-01	0.00E+00	9.24E-03	4.05E-03	1.76E-01	1.80E-01	1.79E+00	6.19E-01	4.96E+00	7.38E+00
300	7.42E-02	0.00E+00	2.64E-03	3.92E-04	6.81E-02	6.85E-02	3.35E-02	1.61E-01	0.00E+00	1.95E-01
1000	9.26E-03	0.00E+00	0.00E+00	0.00E+00	7.67E-03	7.67E-03	0.00E+00	2.00E-02	0.00E+00	2.00E-02

Table 3-14: Liquid source dose rates for 5 µl drop at various layers [rad/hr]

Density Thickness	Ba-133	C-14	Sr-90	Co-60			Cs-137			
[mg/cm^2]	Gamma	Beta	Beta	Beta	Gamma	Total	Beta	Gamma	CE	Total
7	8.91E-05	4.06E-04	1.36E-03	2.12E-03	3.25E-04	2.45E-03	3.55E-02	7.60E-04	1.02E-02	4.65E-02
30	6.35E-05	0.00E+00	8.50E-04	2.76E-04	2.72E-04	5.47E-04	1.40E-02	6.12E-04	7.80E-03	2.24E-02
50	4.90E-05	0.00E+00	6.09E-04	4.03E-05	2.42E-04	2.82E-04	6.33E-03	5.24E-04	6.15E-03	1.30E-02
100	2.93E-05	0.00E+00	3.22E-04	4.02E-06	1.78E-04	1.82E-04	1.14E-03	3.29E-04	2.75E-03	4.22E-03
300	7.39E-06	0.00E+00	5.81E-05	5.00E-07	7.04E-05	7.09E-05	1.87E-05	8.36E-05	0.00E+00	1.02E-04
1000	1.04E-06	0.00E+00	8.38E-09	0.00E+00	8.70E-06	8.70E-06	0.00E+00	1.03E-05	0.00E+00	1.03E-05

Table 3-15: Liquid source dose rates for 10 µl drop at various layers [rad/hr]

Density Thickness	Ba-133	C-14	Sr-90	Co-60			Cs-137			
[mg/cm^2]	Gamma	Beta	Beta	Beta	Gamma	Total	Beta	Gamma	CE	Total
7	1.48E-04	6.07E-04	2.26E-04	3.23E-03	5.88E-04	3.82E-03	5.65E-02	1.36E-03	1.73E-02	7.51E-02
30	1.09E-04	0.00E+00	1.44E-04	4.24E-04	4.92E-04	9.17E-04	2.22E-02	1.10E-03	1.30E-02	3.63E-02
50	8.43E-05	0.00E+00	1.05E-04	6.49E-05	4.37E-04	5.02E-04	1.01E-02	9.13E-04	1.02E-02	2.12E-02
100	5.25E-05	0.00E+00	5.75E-05	6.83E-06	3.50E-04	3.56E-04	1.86E-03	5.87E-04	4.39E-03	6.84E-03
300	1.50E-05	0.00E+00	1.10E-05	7.66E-07	1.33E-04	1.34E-04	4.07E-05	1.63E-04	0.00E+00	2.04E-04
1000	2.00E-06	0.00E+00	0.00E+00	0.00E+00	1.61E-05	1.61E-05	0.00E+00	2.03E-05	0.00E+00	2.03E-05

4.0 Nuclide Information

Five different radionuclides were used in this research. Basic properties of each are provided in Table 4-1. The beta spectra that were used in the MCNP modeling are provided in Figures 4-1 to 4-5.

Table 4-1: Radionuclide information

Radionuclide	Half-Life [Year]	Emission	Yield [%]	Energy [keV]
Co-60	5.27	Gamma #1	99.85	1173
		Gamma #2	99.98	1332
		Beta	100	Avg = 96.4 Max = 1491.4
Cs-137	30.1	Gamma #1	85.10	661.6
		CE	7.79	624.2
		Beta	100	Avg = 187.1 Max = 1175.6
Ba-133	10.5	Gamma #1	62.05	356
		Gamma #2	18.33	302.8
		Gamma #3	34.1	80.9
		Gamma #4	8.94	383.8
		Gamma #5	7.164	276
C-14	5730	Beta	100	Avg = 49.4 Max = 156.4
Sr-90/Y-90	28.5	Beta	100	Avg = 195.8 & 933.6 Max = 546 & 2280

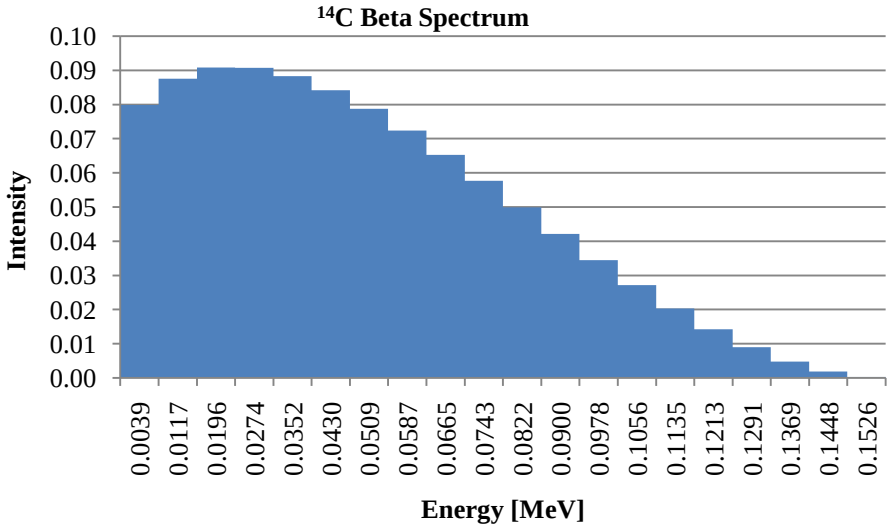

Figure 4-1: C-14 beta spectrum

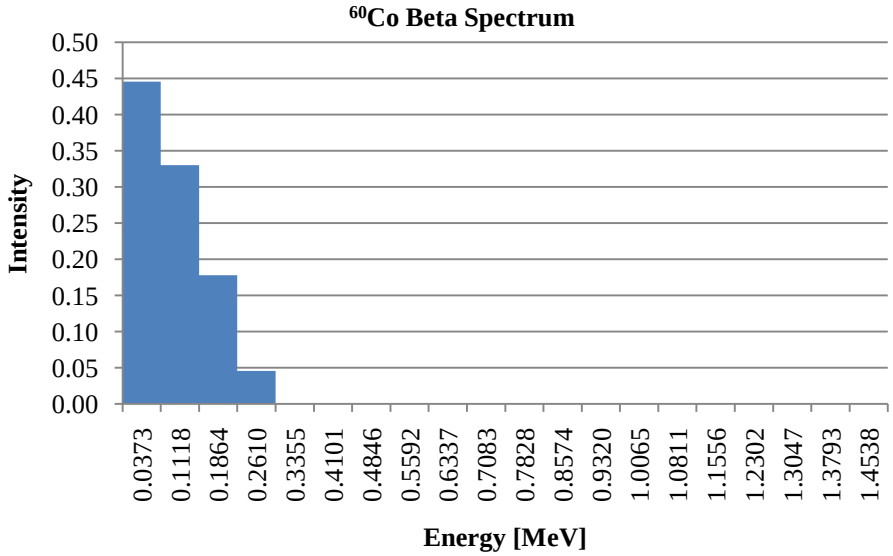

Figure 4-2: Co-60 beta spectrum

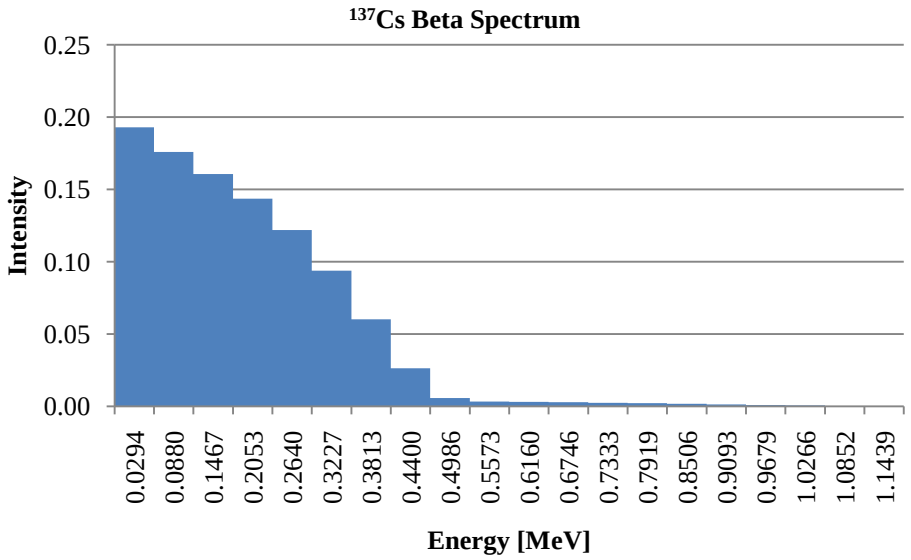

Figure 4-3: Cs-137 beta spectrum

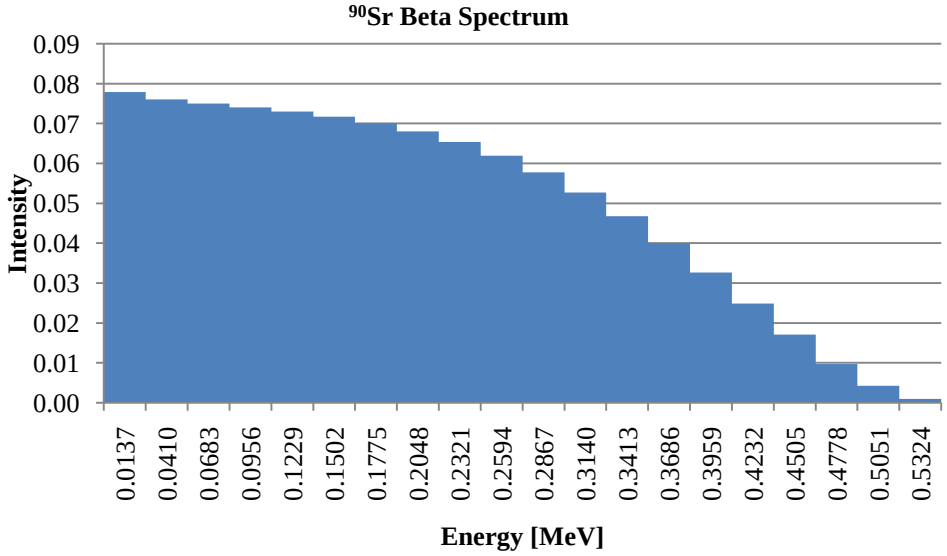

Figure 4-4: Sr-90 beta spectrum

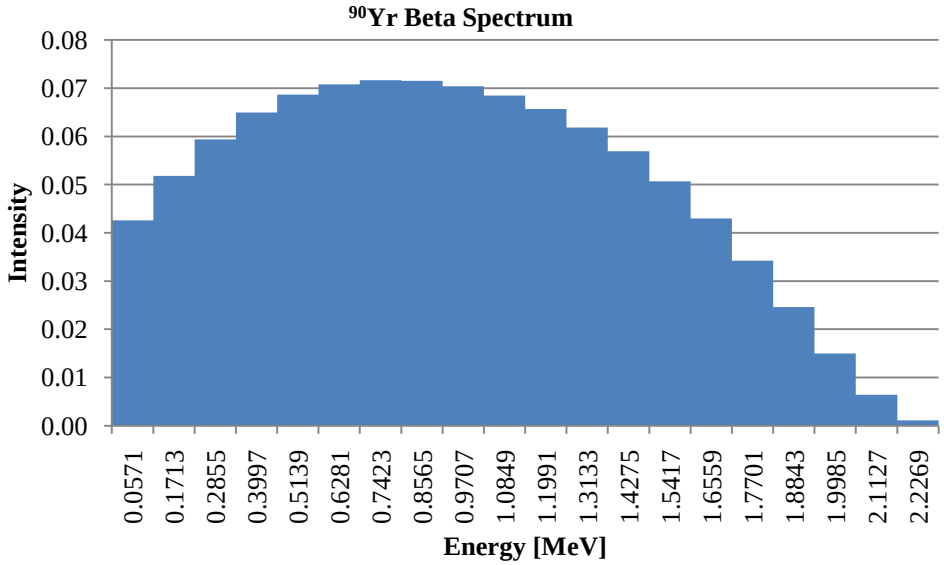

Figure 4-5: Y-90 beta spectrum

5.0 Experimental

5.1 Processing TLDs

Processing TLDs involves an annealing process prior to exposure to completely zero the TLD chip. The LiF TLD-100s are annealed for 1 hour at 400 °C. The TLD chips are then exposed to a radiation source, followed by a post-irradiation anneal. The post-irradiation anneal is used to remove lightly trapped residuals and is done for 10 minutes at 100 °C. The TLD chips are then read in the TLD reader immediately following the post-irradiation anneals. Prior to processing TLD chips, the reader is purged with nitrogen gas for 30 minutes to remove possible charge accumulation inside the reading chamber. Once the system has been purged, 10 dark and 10 light current readings are taken to note system stability.

The TLD chips are processed by placing an individual chip on the planchet and closing the TLD tray door. Approximately 30 seconds is allotted for the system to purge prior to pressing the read button. The read button initiates the heating of the planchet. The TLD reader is set to record the total photon emissions from the TLD chip for a planchet temperature of 100 °C to 240 °C. The optimum temperature for TLD-100s is 195 °C; therefore, this temperature integration range is appropriate. A single digital display provides the TLD output (in Coulombs). After all the TLD chips have been processed, another 10 dark and 10 light current readings are taken to confirm stabilization of the reader during the TLD readout process.

5.2 Experimental Setup

Rectangular Plexiglas stands were used to minimize backscatter to the TLD chip. To ensure a uniform irradiation of every chip, a TLD chip outline was drawn on a sheet of paper to act as a placement jig for both the chip and the source. Figure 5-1 is a photo of the experimental setup with a layer of plastic.

Figure 5-1: Experimental setup without source

Varying amounts of plastic were placed between the chip and source to simulate different thicknesses of skin. To achieve various simulated depths, a variety of plastic types were utilized (Table 5-1). Table 5-2 provides the combination of plastic types that were used to obtain the desired depths along with the percent error for the density thickness layer. The percent was determined as the thickness that differed from the exact depths of interests i.e. 7, 30, 50, 100, 300, and a 1000 mg/cm^2. Errors in thickness due to the available sizes of plastic sheets from the manufacture and the tolerance of the plastic sheets were provided by the manufacturer (McMaster 2009). Figure 5-2 is a photo of the experimental setup with the source in position.

Table 5-1: Types of plastic used in experiment

Material	Density [g/cm^3]	Thickness [cm]	Density Thickness [mg/cm^2]
Polyester	1.4	0.00508	7.1
Polycarbonate #1	1.2	0.0254	30.5
Polycarbonate #2	1.2	0.0762	91.4
Freezer Bag (Glad)	0.94	0.007620	7.2
Sandwich Bag (Glad)	0.94	0.002921	2.7
Cellophane	0.94	0.00127	1.2

Table 5-2: Plastic combinations

Density Thickness [mg/cm^2]	Material	Number of Layers	Density Thickness [mg/cm^2]	Percent Error [%]
0	None	None	None	0
7	Polyester	1	7.1	1.4
30	Polycarbonate #1	1	30.5	1.6
50	Polyester Polycarbonate #1 Freezer Bag	2 1 1	51.8	3.7
100	Polyester Polycarbonate #2 Sandwich Bag	1 1 1	101.2	1.2
300	Polycarbonate #1 Polycarbonate #2	1 3	304.68	1.6
1000	Polycarbonate #2	11	1005.4	0.54

Figure 5-2: Experimental setup with source in position

5.3 Experiment

Solid sources and liquid sources were tested initially to determine the efficiency of the research. An initial batch of 50 LiF TLD-100s were ordered and used to determine the technique and process for further experimentation. The initial 50 TLD chips underwent quality assurance testing and were used to build a calibration curve for the Cs-137 solid source. The Cs-137 solid source experiment was carried out with different density thicknesses and the results proved to be promising for furthering the study. Of the 50 TLD chips, only 32 passed the 30 percent quality assurance

variability criteria imposed on the chip response. Of the 32 remaining chips, only 6 chips were left after constructing the calibration curve and performing the experiments: this reduction in chips was due to chip breakage and loss of the very thin TLD chips.

A second batch of 300 LiF TLD-100s was ordered to continue the research for solid sources and for liquid sources. Table 5-3 displays information on the liquid sources.

Table 5-3: Liquid source information

Source	Chemical Form	Activity [µCi]	Amount [mL]	Activity in 5 µL [µCi]
Co-60	Cobaltous Chloride	1	5	2.0E-04
Cs-137	Cesium Chloride	5	5	1.0E-03
Sr-90	Strontium Chloride	0.1	5	2.0E-05
Ba-133	Barium Chlordie	1	5	2.0E-04
C-14	Sodium Carbonate	10	5	2.0E-03

The smallest volume increment on the pipette available in the department was a 5 µL dispenser. The objective was to simulate a hot particle point source relative to the size of the TLD chip. The volume equation for a hemisphere was used to determine the radius of the liquid drops with different volume; the drops were then modeled in MCNP5 to determine dose rates to the TLD chips. Figure 5-3 displays the relative size of the liquid drop to the TLD chip (modeled as the yellow square).

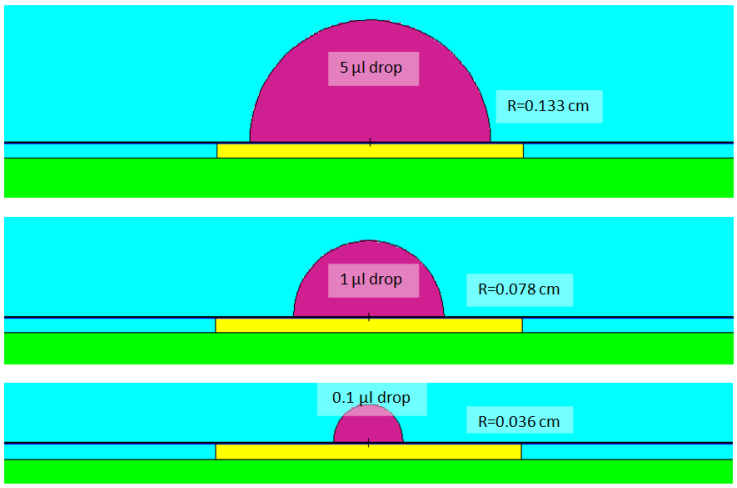

Figure 5-3: Liquid drop models

Due to the small amounts of activity in the 5 µL drops, the necessary irradiation time ranged from 4 days to 2 weeks in order to obtain an adequate dose signal on the TLD chip. Evaporation of the 5 µL drops occurs within about 24 hours. It was assumed initially that the residuals post-evaporation would have somewhat of a uniform distribution.

Based on the Radiochromic film response, we determined that the initial assumption of uniform distribution was inaccurate. Figure 5-4 is a Radiochromic film scan of a uniform distribution and Figure 5-5 is a Radiochromic film scan of a non-uniform distribution. The uniform distribution was obtained from a solid source while the non-uniform distribution was from a liquid source. The Radiochromic film scans were obtained from Thuo (Thuo 2010) with permission.

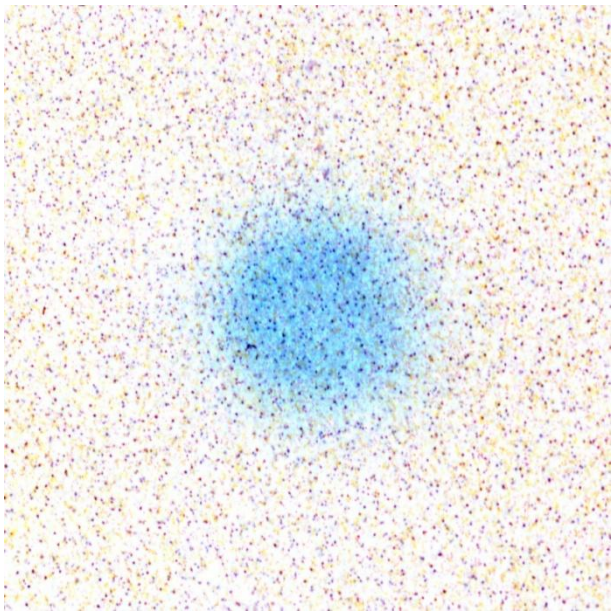

Figure 5-4: Uniform distribution

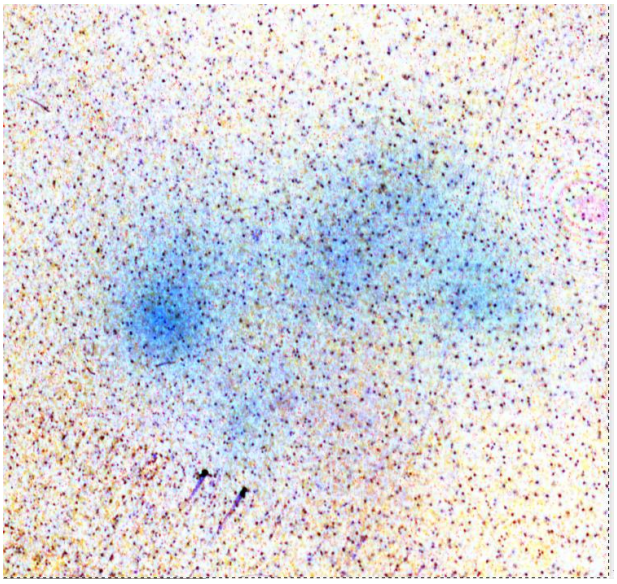

Figure 5-5: Non-uniform distribution

A non-uniform distribution accurately represents hot particle exposure which makes Radiochromic film ideal for further analysis with liquid sources; however, TLD chips, which report only a single value output, are inadequate. The non-uniform source distribution will introduce another source of error on the TLD chips, since it

will be impossible to know how the liquid residuals are finally deposited in relation to the TLD chip.

A possible solution to the non-uniform distribution would be to use much smaller drops of liquid source. The TLD chip with a near-true point source positioned on its centerline would not be as affected by a non-uniform exposure. Problems with this solution involve obtaining very fine and accurate pipettes for dispensing volumes of liquid less than 5 μL. Time is also a problem with smaller drops due to the lower amounts of activity present; therefore, irradiation times would require months to achieve detectable dose signals on the TLD chips. This could be avoided by using more concentrated solutions. Another possible solution would be to devise a chemical composition that would provide more uniform distribution post evaporation.

Due to the non-uniform distribution of the source material within the liquid drops, it was decided to halt the liquid source experiments; therefore, this research focuses on solid sources.

5.4 Calibration Curves

Calibration curves were constructed for the TLDs exposed to each of the five sources. The calibration curve is the TLD output (in Coulombs) verses the delivered dose (in rads). The on-contact dose rate was determined with MCNP and was used to establish the delivered dose. A total of 5 TLD chips were used at each delivered dose interval to account for statistical variability in the TLD chips; however, only 3 TLD chips were used for the Sr-90 source due to the long irradiation time. The software program Matlab was used to obtain the linear fits for each calibration curve.

The Cs-137 calibration curve data displays saturation in the TLD output occurring at approximately 1 rad. A single linear fit is inadequate at low doses due to resulting negative results; therefore, two linear fits were implemented. Figure 5-6 displays the calibration curve data for the Cs-137 source. Figure 5-7 provides the calibration curve through the lower dose region (less than 1 rad). Figure 5-8 provides the calibration

curve for the higher dose region (greater than 1 rad). If the TLD output is less than 2 nC, then the calibration curve for lower dose is used, otherwise the higher dose curve is used. Figures 5-9 to 5-12 display the calibration curves for the other sources. Table 5-4 provides the calibration curve fits.

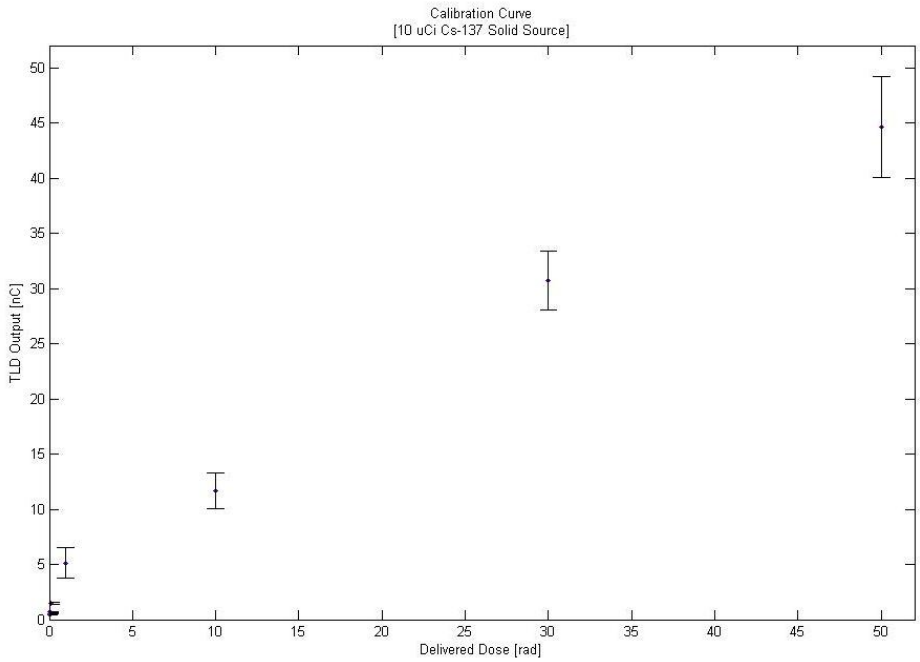

Figure 5-6: Cs-137 solid source calibration curve data

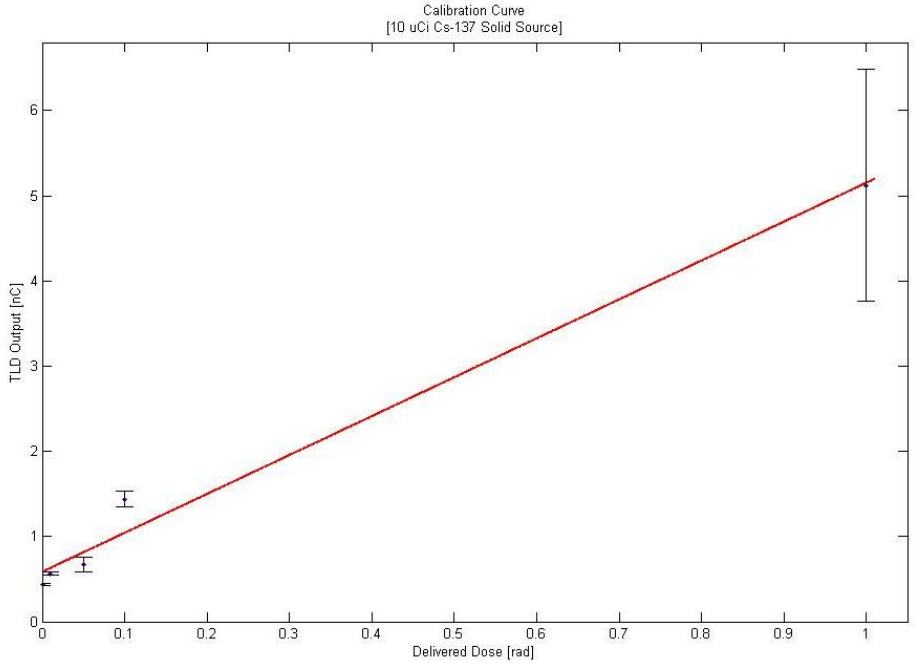

Figure 5-7: Cs-137 solid source lower dose calibration curve

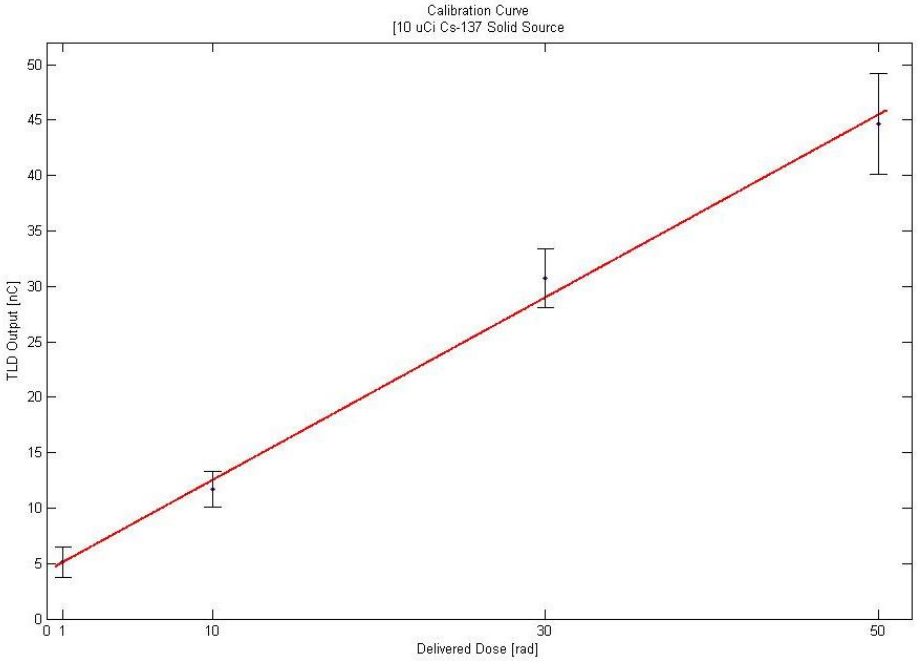

Figure 5-8: Cs-137 solid source higher dose calibration curve

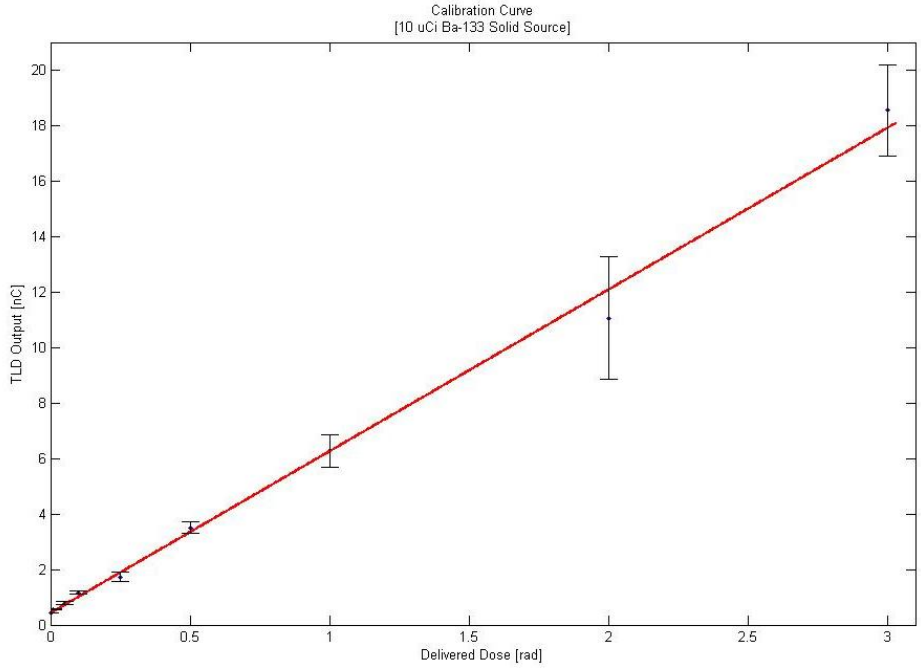

Figure 5-9: Ba-133 solid source calibration curve

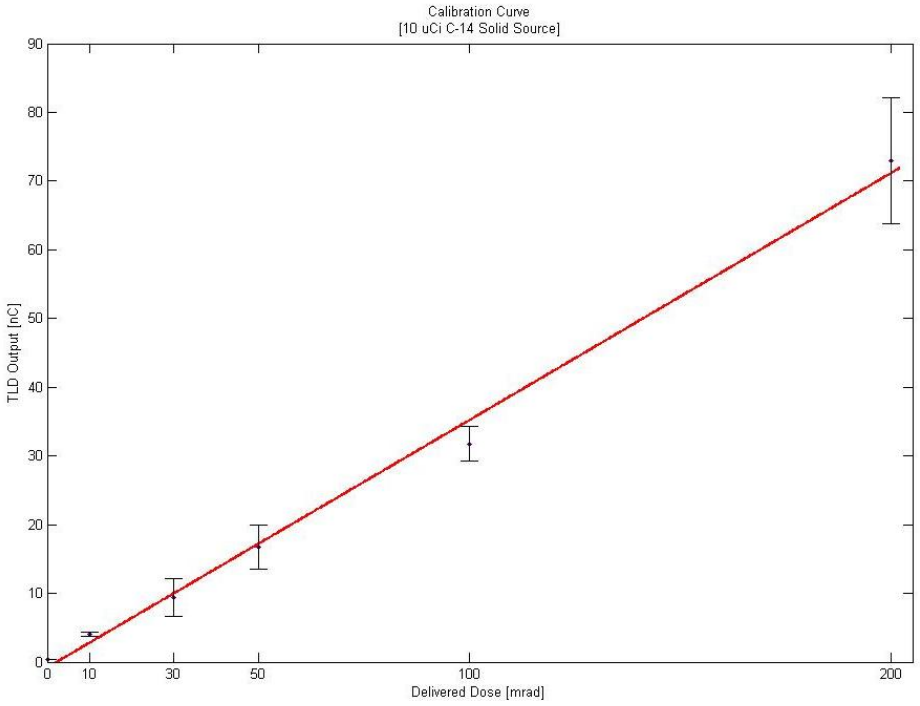

Figure 5-10: C-14 solid source calibration curve

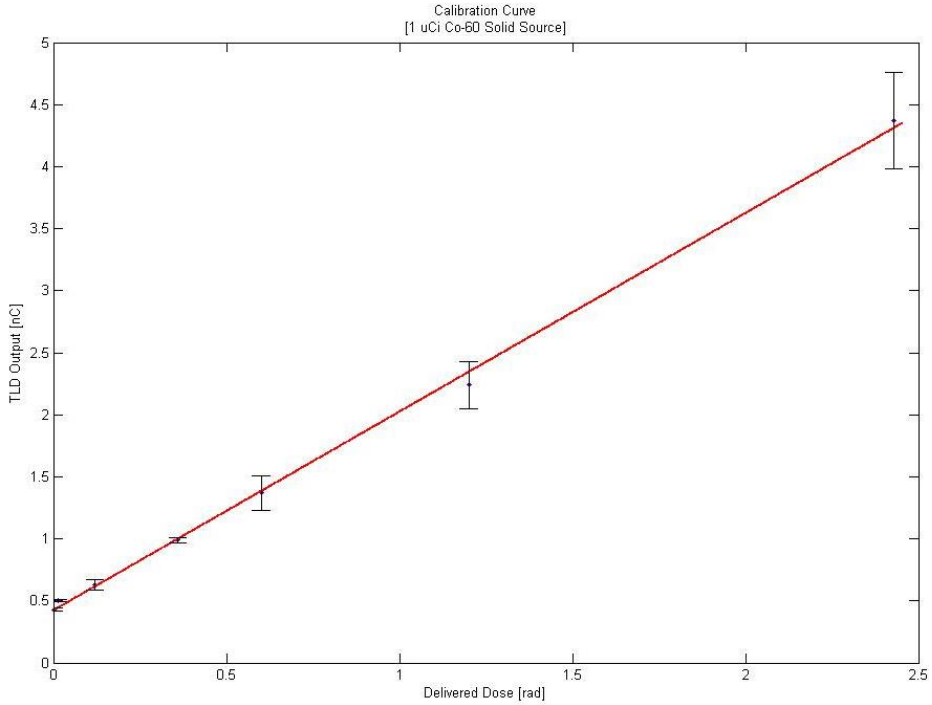

Figure 5-11: Co-60 solid source calibration curve

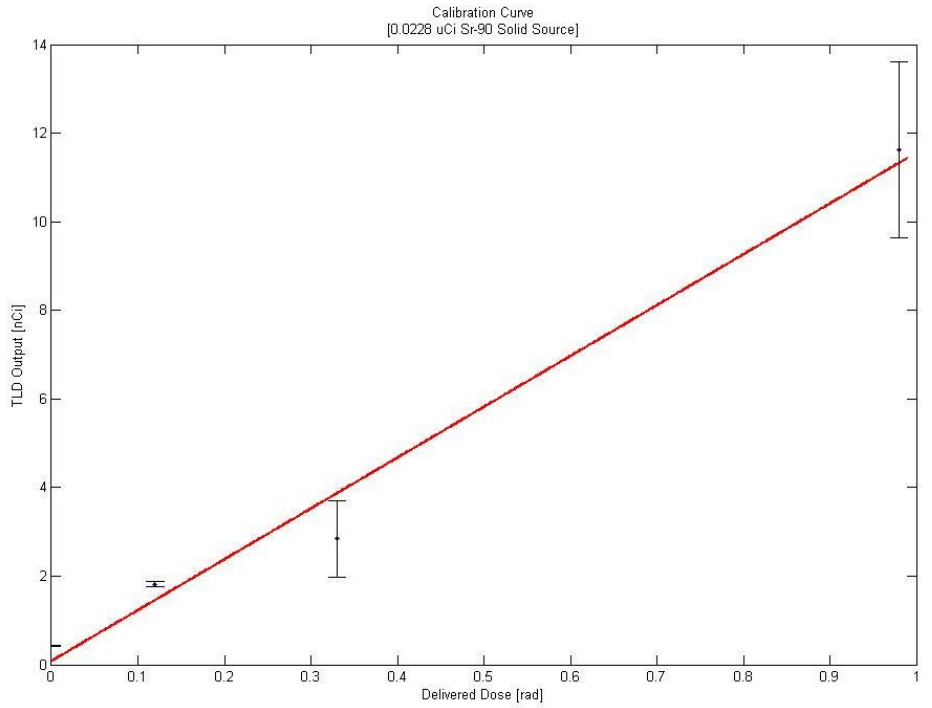

Figure 5-12: Sr-90 solid source calibration source

Table 5-4: Calibration curve equation fits

Nuclide	Fit	R^2
Cs-137 (Lower)	Y=4.6x+0.59	0.97
Cs-137 (Higher)	Y=0.82x+4.3	0.97
Ba-133	Y=5.8x+0.42	0.97
Co-60	Y=1.6x +0.42	0.98
C-14	Y=0.36x-0.84	0.97
Sr-90	Y=11.44x+0.1883	0.94

5.5 Experimental TLD Data

The experiments were performed by irradiating an individual TLD chip with a layer of plastic equivalent tissue at a thickness corresponding to a desired density thickness between the TLD chip and source. A total of 5 TLD chips were irradiated at each density thickness to account for TLD chip statistical variability; however, only 3 TLD chips per density thickness were used for Sr-90, due to long irradiation times required for Sr-90. Figures 5-13 to 5-17 display the experimental and the MCNP expected data. The red fit is the MCNP exponential fit and the black fit is the experimental data exponential fit.

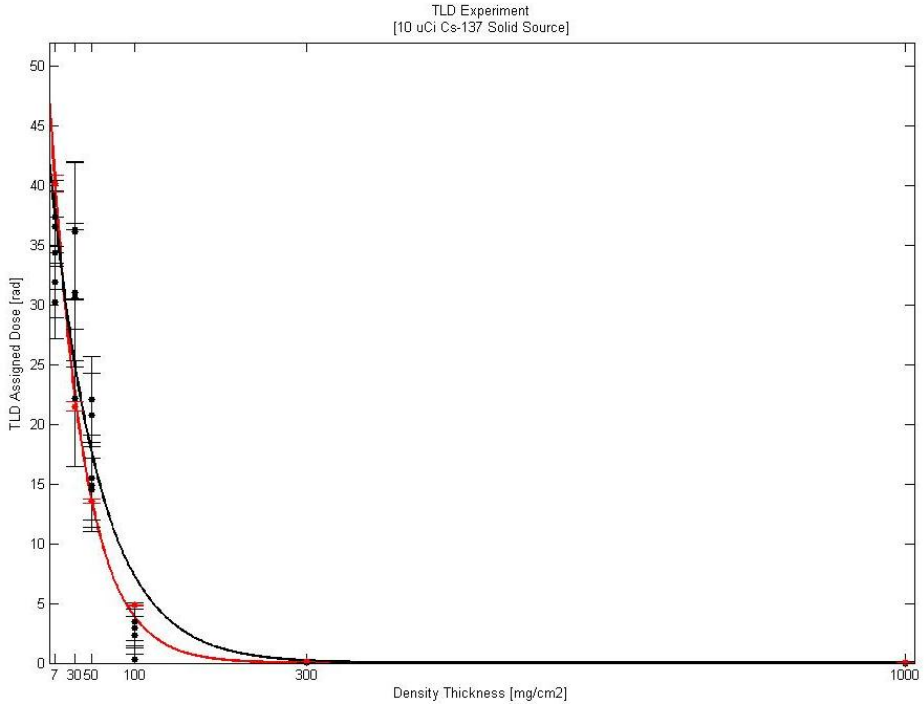

Figure 5-13: Cs-137 experimental and MCNP expected data

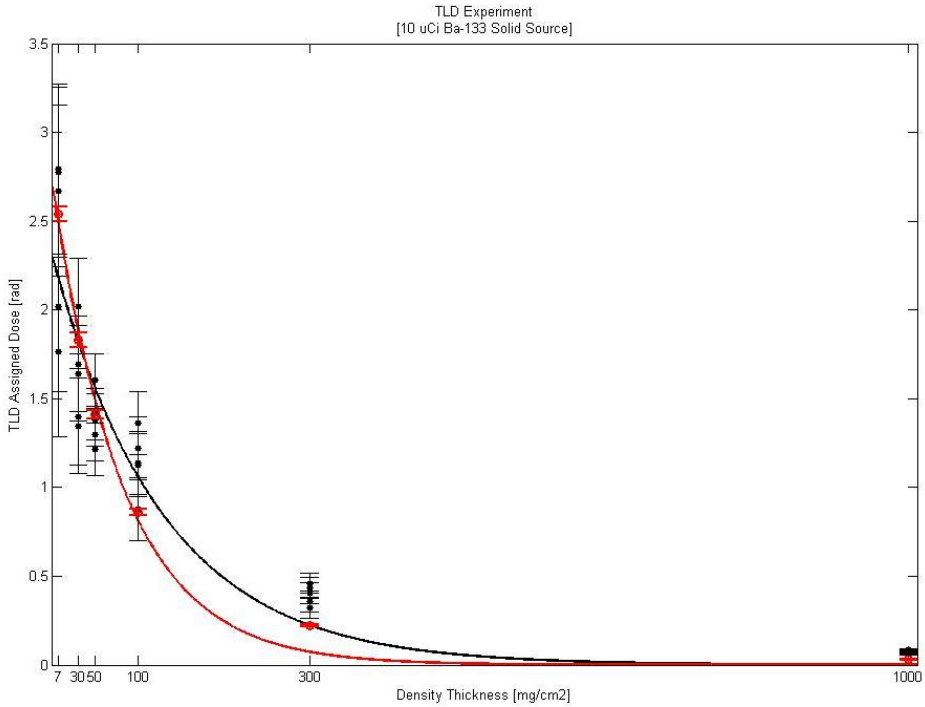

Figure 5-14: Ba-133 experimental and MCNP expected data

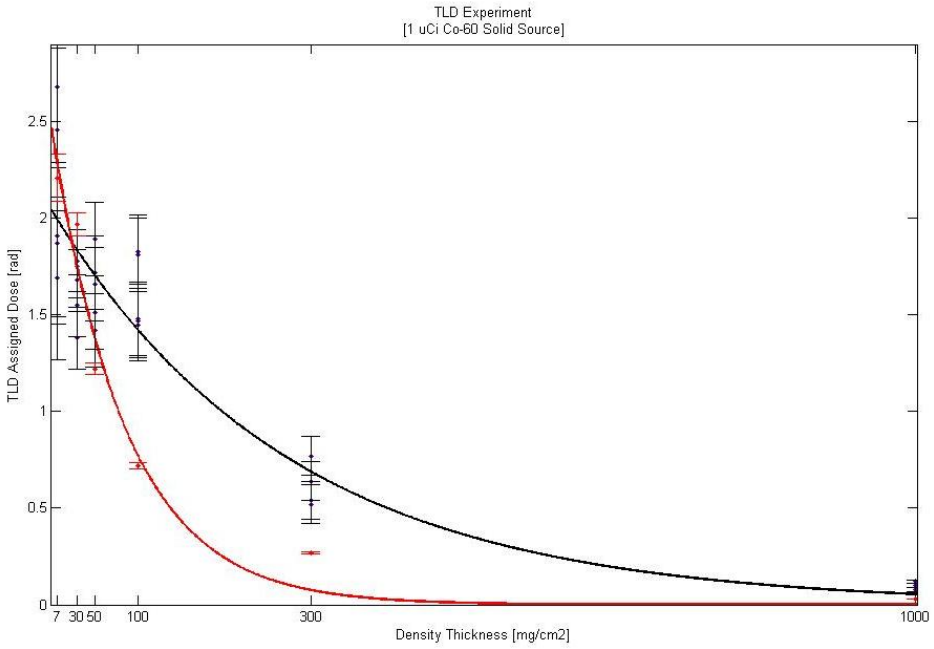

Figure 5-15: Co-60 experimental and MCNP expected data

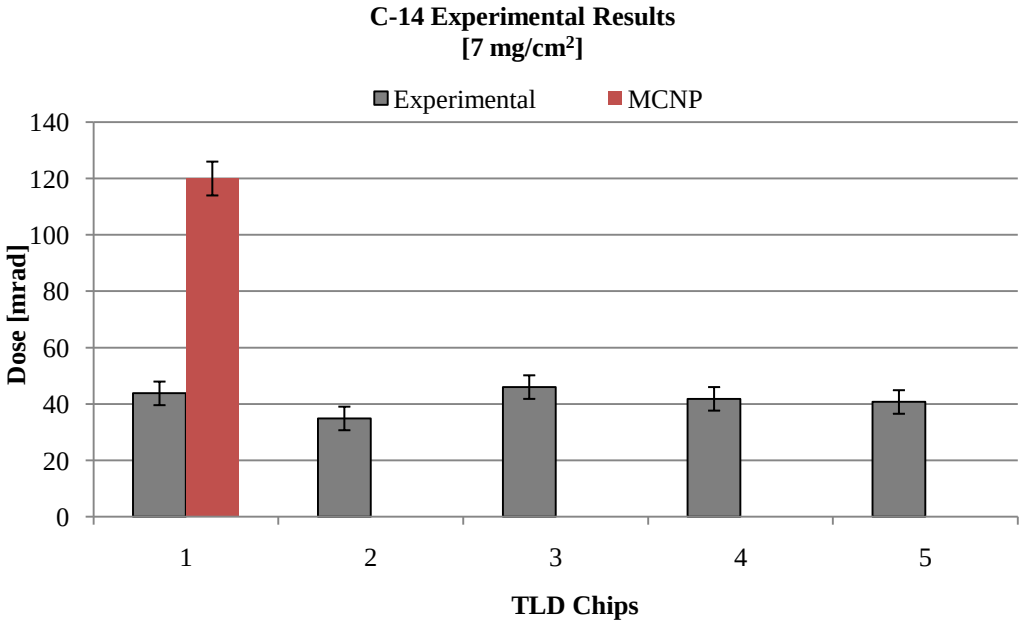

Figure 5-16: C-14 experimental and MCNP expected data

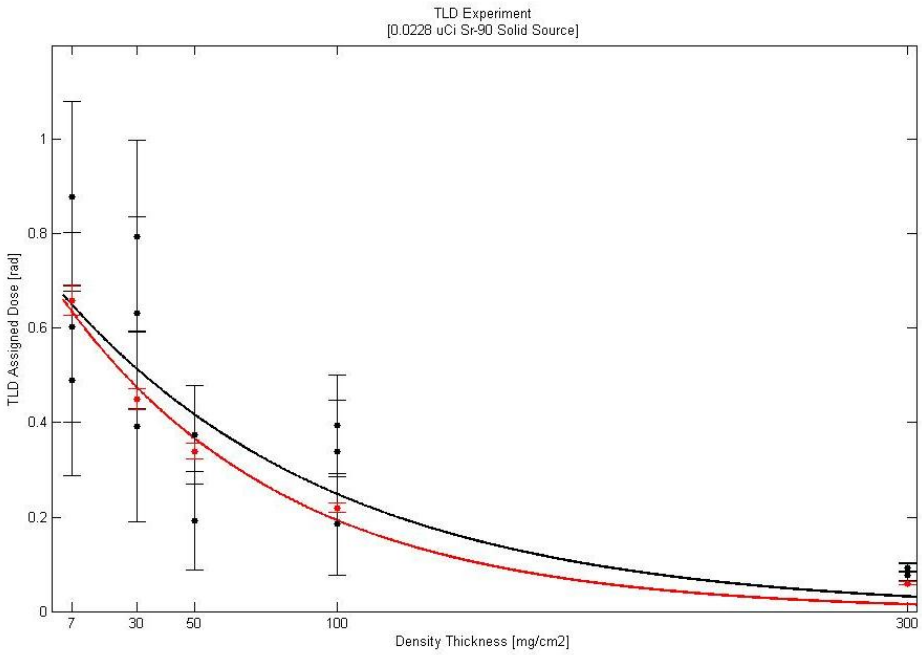

Figure 5-17: Sr-90 experimental and MCNP expected data

The Ba-133 and Cs-137 experiments are close to the expected MCNP values. The Co-60 experimentally determined dose was much greater than the MCNP dose values. The C-14 experimental data was about half of the MCNP expected value. The experimental and MCNP data fits are provided in Table 5-5. The coefficients A and B for the chip integration results pertain to Eqn. (5.1).

$$Y = Ae^{Bx} \tag{5.1}$$

Table 5-5: Experimental data and MCNP data fits

Nuclide	Experimental Fit		R^2	MCNP Fit		R^2
	A	B		A	B	
Cs-137	4.2E+01	-1.8E-02	0.9	4.8E+01	-2.5E-02	0.99
Co-60	2.0E+00	-3.6E-03	0.89	2.5E+00	-1.2E-02	0.97
Ba-133	2.3E+00	-7.7E-03	0.88	2.7E+00	-1.2E-02	0.99
Sr-90	7.0E-01	-1.0E-02	0.64	7.0E-01	-1.3E-02	0.98

6.0 Calculations

6.1 MCNP Calculations

The output from the MCNP5 *F8 tally is given in MeV per particle. The following examples are provided for calculating dose at the 7 mg/cm^2 layer with a 10 μCi Cs-137 source.

Beta:

MCNP Output = 7.51E-3 MeV/D

$$\frac{\left(7.51 \times 10^{-3}\ \left[\frac{MeV}{D}\right]\right) \times \left(1.602 \times 10^{-13}\left[\frac{J}{MeV}\right]\right) \times \left(3.7 \times 10^{5}\ \left[\frac{D}{s}\right]\right)}{4.06 \times 10^{-6}[kg]}$$

$$= 1.09 \times 10^{-4}\ \frac{J}{kg \cdot\ s}$$

$$1.09 \times 10^{-4}\left[\frac{Gy}{s}\right] \times 100\left[\frac{rad}{Gy}\right]\ \times 3600\left[\frac{s}{hr}\right] = 39.5\ \left[\frac{rad}{hr}\right]$$

Conversion Electron:

MCNP Output = 5.06E-2 MeV/D

$$\frac{\left(5.06 \times 10^{-2}\ \left[\frac{MeV}{D}\right]\right) \times \left(1.602 \times 10^{-13}\left[\frac{J}{MeV}\right]\right) \times \left(3.7 \times 10^{5}\ \left[\frac{D}{s}\right]\right) \times (0.0779[\ yield])}{4.06 \times 10^{-6}[kg]}$$

$$= 7.38 \times 10^{-6}\ \frac{J}{kg \cdot\ s}$$

$$7.38 \times 10^{-6}\left[\frac{Gy}{s}\right] \times 100\left[\frac{rad}{Gy}\right]\ \times 3600\left[\frac{s}{hr}\right] \times = 20.7\left[\frac{rad}{hr}\right]$$

Gamma:

MCNP Output = 3.78E-4 MeV/D

$$\frac{\left(3.78 \times 10^{-4}\ \left[\frac{MeV}{D}\right]\right) \times \left(1.602 \times 10^{-13}\left[\frac{J}{MeV}\right]\right) \times \left(3.7 \times 10^{5}\ \left[\frac{D}{s}\right]\right) \times (0.85[\ yield])}{4.06 \times 10^{-6}[kg]}$$

$$= 5.53\ \times 10^{-6}\ \frac{J}{kg\ \cdot s}$$

$$5.53 \times 10^{-6}\left[\frac{Gy}{s}\right] \times 100\left[\frac{rad}{Gy}\right] \times 3600\left[\frac{s}{hr}\right] = 1.7\left[\frac{rad}{hr}\right]$$

The total dose for the beta, conversion electron, and gamma contributors is 61.9 rad per hour. Cs-137 has a relatively high-abundance conversion electron; therefore, that particular conversation electron was included when determining total dose for the Cs-137 source. The conversion electron has an energy of 624 keV with 7.79 percent abundance, therefore contributing significantly to the shallow dose.

6.2 Hand Calculations

To validate the MCNP and TLD results, rough hand calculations were performed. The following equation was used to calculate the beta and conversion electron dose to the TLD chip. The subscript SE denotes the source encapsulation shielding. The fluence was approximated by 50 percent of the total number of particles emitted by the source; however, as the distance between the source and the TLD chip increases, the fluence decreases and solid angle calculations are required for more accurate results.

$$\frac{\bar{E}[MeV]\times(\#\ of\ Particles\ )[d/s]\times 0.5\times(1.602E{-}13)[J/MeV]}{Mass\ [kg]} \times e_{SE}{}^{(-\rho x\times\mu)} \times e_{skin}{}^{(-\rho x\times\mu)} \qquad (6.1)$$

The value of μ [cm^2/g] for different media is found using (Martin 2006):

$$\mu_{tissue} = 18.6(E_{max} - 0.036)^{-1.37} \qquad (6.2)$$

$$\mu_{air} = 16(E_{max} - 0.036)^{-1.4} \qquad (6.3)$$

$$\mu_{other} = 17(E_{max})^{-1.14} \qquad (6.4)$$

The following equation was used to calculate the gamma dose to the TLD chip, where A and B are attenuation and energy absorption factors respectively.

$$\frac{E[MeV]\times(\#\ of\ Particles\ )[d/s]\times 0.5\times(1.602E{-}13)[J/MeV]}{Mass\ [kg]} \times \mathrm{A} \times \mathrm{B} \qquad (6.5)$$

Eqn. (6.5) without the A and B factors neglects attenuation of the skin and the source encapsulation; therefore, Eqn. (6.6) or the 'A' factor is multiplied by Eqn. (6.5) to account for attenuation. Eqn. (6.5) assumes that 50 percent of the particles will be

completely deposited in the TLD chip; however, the majority of the gamma particles will pass through the chip while only depositing a small fraction of energy. To correct for this, Eqn. (6.5) requires modification – multiplication by Eqn. (6.7) or the 'B' factor. Eqn. (6.7) determines the percent of energy absorbed by the TLD chip.

$$\mathrm{A} = \left[e_{skin}{}^{\left(-\frac{\mu}{\rho}\times\rho x\right)}\right] \times \left[e_{SE}{}^{\left(-\frac{\mu}{\rho}\times\rho x\right)}\right] \tag{6.6}$$

$$B = 1 - e_{TLD}^{\left(\frac{-\mu_{en}}{\rho}\times\rho x\right)} \tag{6.7}$$

The variable μ_{en}/ρ is the linear energy absorption coefficient. Tables 6-1 to 6-3 display the hand calculation results for the various density thicknesses, nuclides, and radiation types. Figures 6-1 to 6-5 display a comparison of hand calculations to MCNP calculations. The hand calculations match within reason to the MCNP results except for the C-14.

Table 6-1: Hand calculations [rad/hr] for sources (beta)

Density Thickness [mg/cm^2]	Cs-137	Co-60	C-14	Sr-90	Y-90
7	4.80E+01	1.32E-01	2.93E-01	1.07E-12	8.11E-02
30	1.82E+01	1.47E-02	0.00E+00	3.79E-13	7.07E-02
50	7.82E+00	2.18E-03	0.00E+00	1.53E-13	6.28E-02
100	9.46E-01	1.85E-05	0.00E+00	1.59E-14	4.66E-02
300	2.04E-04	0.00E+00	0.00E+00	1.86E-18	1.42E-02
1000	0.00E+00	0.00E+00	0.00E+00	3.19E-32	2.21E-04

Table 6-2: Hand calculations [rad/hr] for sources (CE)

Density Thickness [mg/cm^2]	Cs-137
7	1.87E+01
30	8.36E+00
50	4.16E+00
100	7.24E-01
300	6.68E-04
1000	0.00E+00

Table 6-3: Hand calculations [rad/hr] for sources (gamma)

Density Thickness [mg/cm^2]	Cs-137	Co-60	Ba-133
7	1.80E+00	6.50E-01	8.46E-01
30	1.80E+00	6.49E-01	8.44E-01
50	1.80E+00	6.48E-01	8.41E-01
100	1.79E+00	6.46E-01	8.37E-01
300	1.77E+00	6.38E-01	8.18E-01
1000	1.65E+00	6.10E-01	7.54E-01

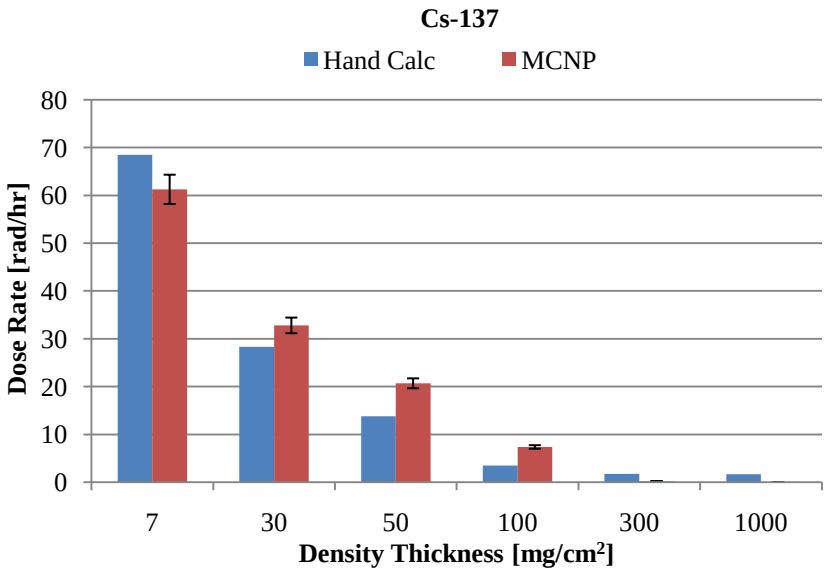

Figure 6-1: Cs-137 hand calculation compared to MCNP

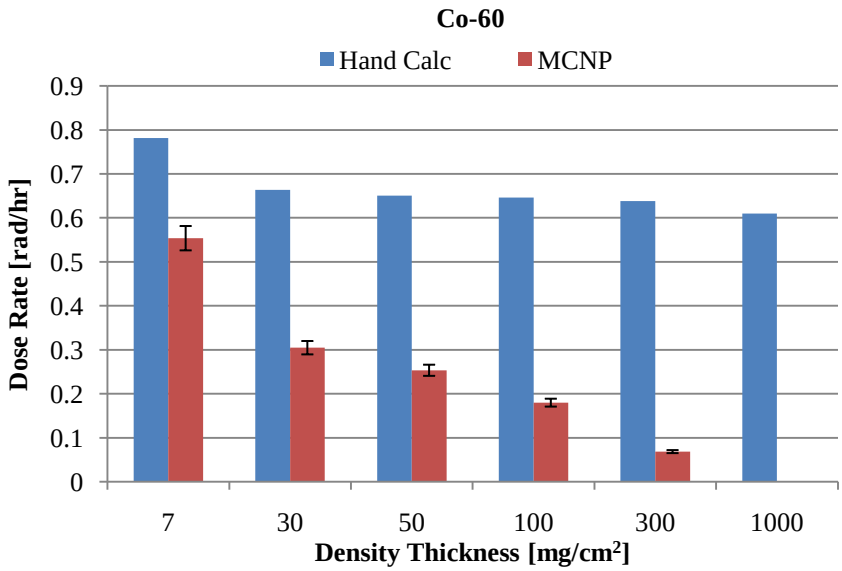

Figure 6-2: Co-60 hand calculation compared to MCNP

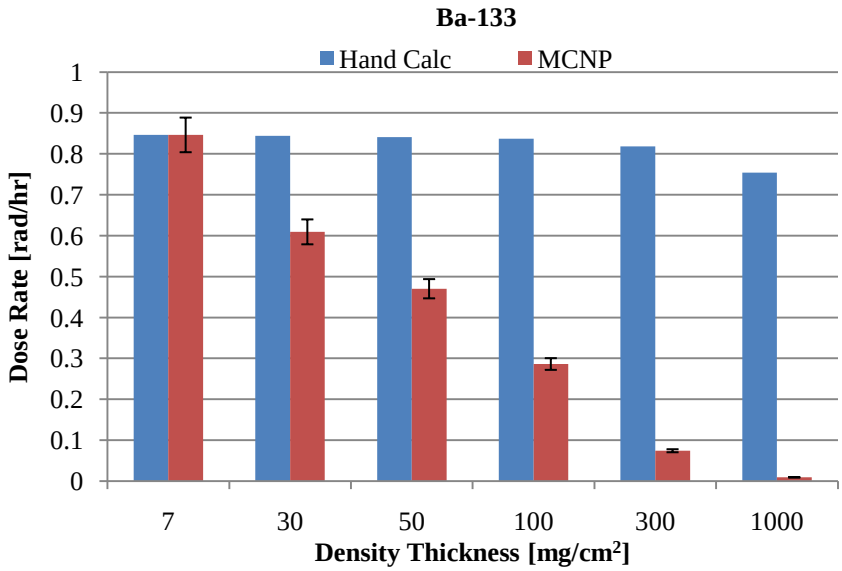

Figure 6-3: Ba-133 hand calculation compared to MCNP

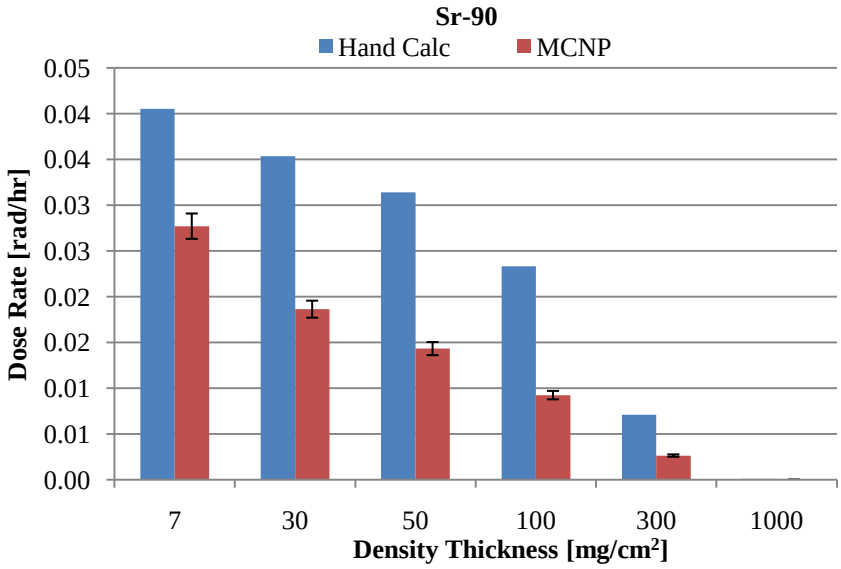

Figure 6-4: Sr-90 hand calculation compared to MCNP

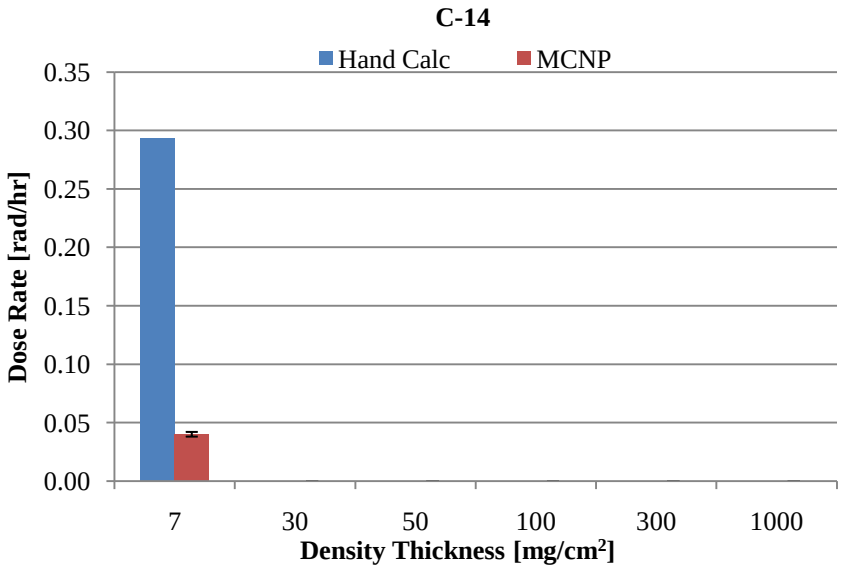

Figure 6-5: C-14 hand calculation compared to MCNP

7.0 Detector

A prototypic skin contamination dosimeter was developed by Oregon State University and is envisioned to allow simultaneous, real-time dose measurements at three depths of interest (Cazalas 2009). The dosimeter uses a combination of scintillators and non-scintillation plastic. The shallow and eye lens dose use a plastic scintillator and the deep dose uses a crystal scintillator (Cazalas 2009). The scintillators and the non-scintillation plastic are both tissue equivalent. A photomultiplier tube is coupled to the assembly. Currently, only a single depth can be monitored at a time due to the pulse shaping analysis of the multiple scintillators. The entire scintillation assembly and PMT are placed within an aluminum tube. A Mylar window covers the detector for blocking ambient light and to act as an inner reflective surface (Cazalas 2009).

8.0 Results

The mean TLD experimental results were used to define a single result value. The standard deviation of the TLDs per data point was used to determine the error for the single reported value. Due to the statistical variations in the TLD chips, the standard deviations are quite large compared to the reported value. Tables 8-1 to 8-5 display the results with the two modification factors for percent deposited within the first 3.79 microns and the area modification from 0.1 cm^2 to 10 cm^2. To account for change in mass a factor of 40 was applied to the depth modifier. The mass of the first 3.79 μm of the TLD chip is 0.0001 g and the total TLD chip is 0.0040 g. A factor of 0.01 is applied to the area modifier to account for the change in mass. The mass of the 10 cm^2 desired area is 0.4012 g, which is a factor of 100 greater than just the 0.1 cm^2 area TLD chip.

Table 8-1: Cs-137 experimental TLD results

Layer [mg/cm^2]	TLD [rad]	± σ [rad]	TLD [nGy/s]	± σ [nGy/s]	Depth Modifier	Area Modifier	Total [nGy/s]	± σ [nGy/s]
7	3.41E+01	3.02E+00	1.44E+05	1.28E+04	1.57E+00	1.16E-02	2.63E+03	2.33E+02
30	3.13E+01	5.74E+00	1.33E+05	2.43E+04	1.47E+00	1.27E-02	2.47E+03	4.53E+02
50	1.76E+01	3.56E+00	7.45E+04	1.51E+04	1.38E+00	1.37E-02	1.41E+03	2.86E+02
100	2.89E+00	1.60E+00	1.22E+04	6.77E+03	1.47E+00	1.66E-02	2.99E+02	1.65E+02
300	7.00E-02	1.70E-02	2.96E+02	7.20E+01	1.13E+00	1.31E-01	4.38E+01	1.06E+01
1000	9.00E-03	2.10E-02	3.81E+01	8.89E+01	1.10E+00	4.98E-01	2.09E+01	4.89E+01

Table 8-2: Co-60 experimental TLD results

Layer [mg/cm^2]	TLD [rad]	± σ [rad]	TLD [nGy/s]	± σ [nGy/s]	Depth Modifier	Area Modifier	Total [nGy/s]	± σ [nGy/s]
7	2.12E+00	3.53E-01	1.47E+03	2.45E+02	2.08E+00	2.65E-02	8.14E+01	1.36E+01
30	1.63E+00	1.36E-01	1.13E+03	9.43E+01	1.20E+00	4.91E-02	6.65E+01	5.54E+00
50	1.63E+00	1.55E-01	1.13E+03	1.07E+02	1.07E+00	5.92E-02	7.15E+01	6.78E+00
100	1.61E+00	1.60E-01	1.12E+03	1.11E+02	1.06E+00	7.69E-02	9.11E+01	9.04E+00
300	6.20E-01	8.31E-02	4.31E+02	5.77E+01	1.07E+00	1.40E-01	6.44E+01	8.63E+00
1000	1.00E-01	1.24E-02	6.94E+01	8.62E+00	1.14E+00	4.94E-01	3.93E+01	4.88E+00

Table 8-3: C-14 experimental TLD results

Layer [mg/cm^2]	TLD [rad]	± σ [rad]	TLD [nGy/s]	± σ [nGy/s]	Depth Modifier	Area Modifier	Total [nGy/s]	± σ [nGy/s]
7	4.15E-02	4.18E-03	3.84E+01	3.87E+00	2.04E+01	1.00E-02	7.84E+00	7.91E-01

Table 8-4: Ba-133 experimental TLD results

Layer [mg/cm^2]	TLD [rad]	± σ [rad]	TLD [nGy/s]	± σ [nGy/s]	Depth Modifier	Area Modifier	Total [nGy/s]	± σ [nGy/s]
7	2.40E+00	4.79E-01	2.23E+03	4.44E+02	1.12E+00	3.10E-02	7.74E+01	1.54E+01
30	1.62E+00	2.69E-01	1.50E+03	2.49E+02	1.10E+00	3.80E-02	6.28E+01	1.04E+01
50	1.38E+00	1.47E-01	1.28E+03	1.36E+02	1.09E+00	4.52E-02	6.30E+01	6.71E+00
100	1.15E+00	1.77E-01	1.06E+03	1.64E+02	1.08E+00	6.42E-02	7.33E+01	1.13E+01
300	3.96E-01	5.75E-02	3.67E+02	5.33E+01	1.02E+00	1.58E-01	5.94E+01	8.63E+00
1000	7.38E-02	7.45E-03	6.83E+01	6.90E+00	1.04E+00	5.09E-01	3.63E+01	3.66E+00

Table 8-5: Sr-90 experimental TLD results

Layer [mg/cm^2]	TLD [rad]	± σ [rad]	TLD [nGy/s]	± σ [nGy/s]	Depth Modifier	Area Modifier	Total [nGy/s]	± σ [nGy/s]
7	6.60E-01	2.01E-01	7.64E+01	2.32E+01	1.33E+00	3.57E-01	3.62E+01	1.10E+01
30	6.10E-01	2.02E-01	7.06E+01	2.34E+01	1.22E+00	3.68E-01	3.45E+01	1.14E+01
50	2.60E-01	1.04E-01	3.01E+01	1.21E+01	1.20E+00	3.76E-01	1.38E+01	5.52E+00
100	3.10E-01	1.08E-01	3.59E+01	1.25E+01	1.12E+00	3.80E-01	1.64E+01	5.72E+00
300	9.00E-02	9.70E-03	1.04E+01	1.12E+00	1.13E+00	3.85E-01	4.49E+00	4.84E-01

An MCNP skin model was written using tissue equivalent plastic as the material for the simulated skin depth. Dose was determined to a layer of 1 mg/cm^2 with an area of 10 cm^2, which is equivalent to the area and density thickness for dose reporting. The MCNP skin model was developed to use the same source configurations as the TLD chip MCNP models, thus eliminating additional variables. Tables 8-6 to 8-10 display the numerical results of experimental data, VARSKIN, MCNP Skin model, and the prototype detector for each of the sources. Figures 8-1 to 8-5 graphically display the experimental data, MCNP skin model, VARSKIN, and prototype detector for each of the sources.

The VARSKIN version 3 disk source parameters only computes a photon dose with a diameter of less than 1 mm; however, the sources used in this research had a 2.5

mm diameter. The VARSKIN results include attenuation by the source window and are modeled with a disk source for the beta particles and a point source for the photons.

Table 8-6: Cs-137 result comparison

Cs-137 Layer [mg/cm^2]	TLDs Dose [nGy/s]	MCNP (Skin) Dose [nGy/s]	VARSKIN Dose [nGy/s]	Detector Dose [nGy/s]
7	2630 ± 233	3890 ± 195	2079	1900 ± 8.9
30	2470 ± 453	2200 ± 110	839	na
50	1410 ± 286	1440 ± 72.1	424	na
100	299 ± 165	653 ± 32.7	192	708 ± 17
300	44 ± 10.6	103 ± 5.15	106	75.2 ± 6.7
1000	21 ± 48.9	40.4 ± 2.02	43	34.5 ± 1.7

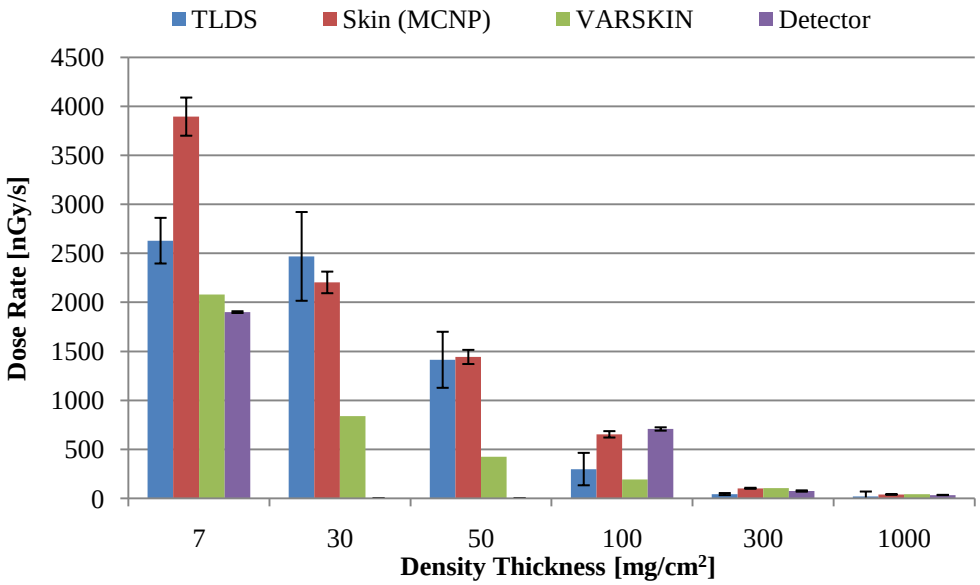

Figure 8-1: Cs-137 result comparison

The Cs-137 results for the TLD chips are relatively close to the modeled MCNP skin values. All four methods matched well for the 1000 mg/cm^2 depth. The main mode of decay contributing to the dose at the 1000 mg/cm^2 depth is gamma radiation. The Co-60 results were very close at the 7 mg/cm^2 depth for all four methods. At depths greater than 100 mg/cm^2 the TLD chips are slightly higher than the other three

methods. This could be attributed to the calibration curve and saturation in the TLD with doses in excess of 1 rad.

Table 8-7: Co-60 result comparison

Co-60 Layer [mg/cm^2]	TLDs Dose [nGy/s]	MCNP (Skin) Dose [nGy/s]	VARSKIN Dose [nGy/s]	Detector Dose [nGy/s]
7	81.4 ± 13.6	96.3 ± 4.82	77	81 ± 2.6
30	66.5 ± 5.54	68.6 ± 3.43	71	na
50	71.5 ± 6.78	63.8 ± 3.19	67	na
100	91.1 ± 9.04	59.1 ± 2.95	59	49.9 ± 6.2
300	64.4 ± 8.63	41.0 ± 2.05	40	32.7 ± 4.9
1000	39.3 ± 4.88	16.9 ± 0.85	16	13.2 ± 1.9

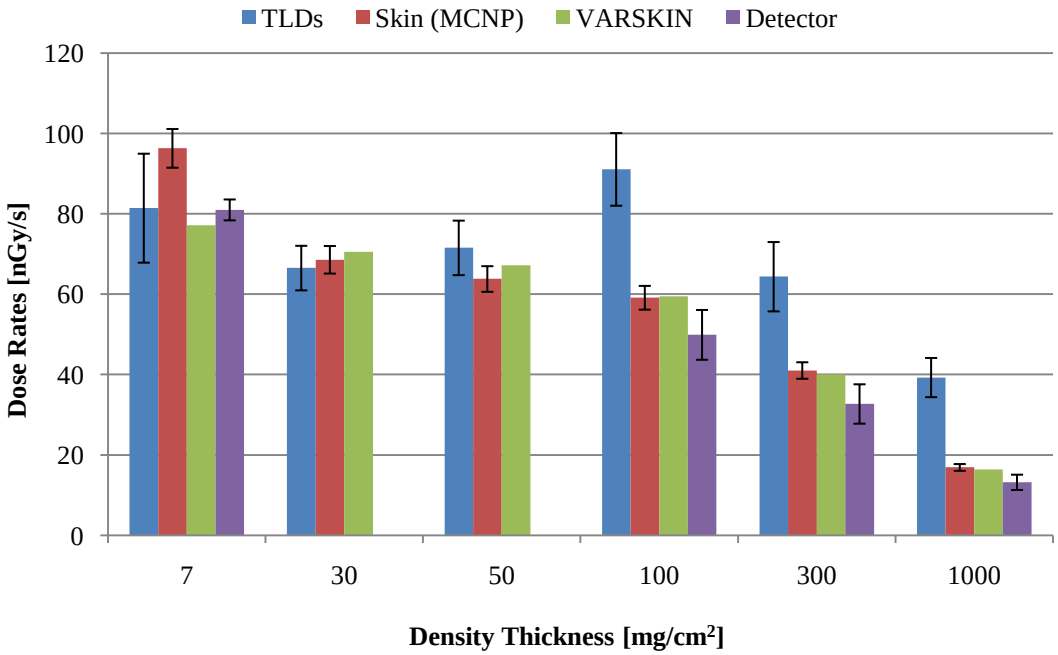

Figure 8-2: Co-60 result comparison

Table 8-8: C-14 result comparison

C-14	TLDs	MCNP (Skin)	VARSKIN	Detector
Layer [mg/cm^2]	Dose [nGy/s]	Dose [nGy/s]	Dose [nGy/s]	Dose [nGy/s]
7	7.84 ± 0.79	28.2 ± 1.41	0	271 ± 1.5

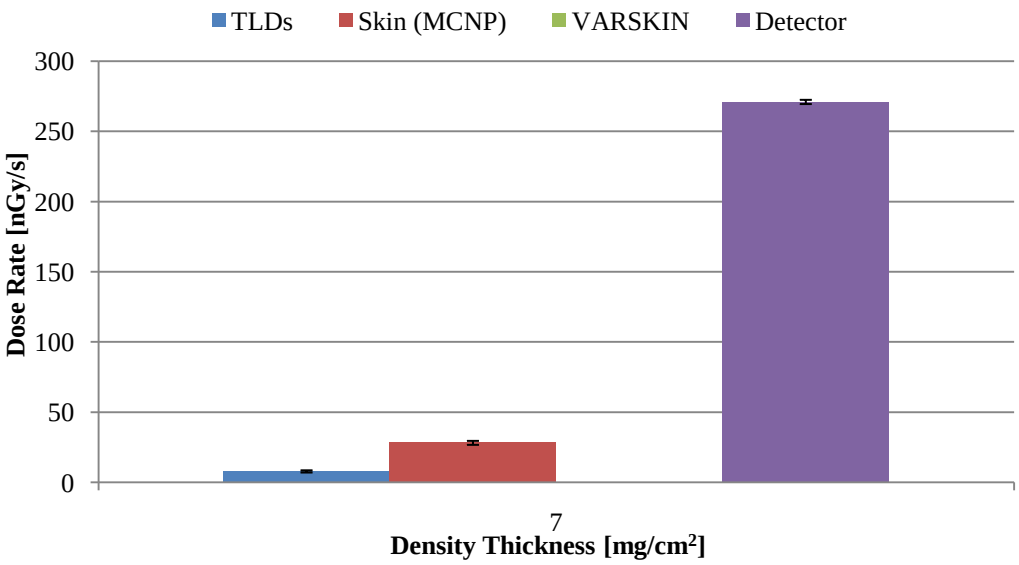

Figure 8-3: C-14 result comparison

The results for C-14 were the most varied among the methods. VARSKIN reports a value of 0 nGy/s at the 7 mg/cm^2 with the source window layer added for attenuation; however, the TLDs report a dose of approximately 0.25 of the MCNP skin model. The prototype detector results are an order of magnitude higher than the MCNP skin results.

The difference between the MCNP skin model and the TLD results may be attributed to the low energy beta particles and the anneal procedure for the TLD chips. The post-irradiation anneal may be removing some of the low energy electron traps created by the low energy beta particles. Further research would have to be conducted

to determine if this is indeed the cause in the discrepancy. It should be noted that all the TLDs regardless of the type of source were subjected to the same anneal procedures to minimize possible variables. The difference between the prototype detector and the MCNP skin model suggests that the C-14 source may be modeled with too thick of a source window. The source dimensions were obtained from the manufacturer; however, it is possible the dimensions are not correct, and due to the low energy beta particles, any slight variation in window thickness will have an enormous impact on attenuation.

Table 8-9: Ba-133 result comparison

Ba-133 Layer [mg/cm^2]	TLDs Dose [nGy/s]	MCNP (Skin) Dose [nGy/s]	VARSKIN Dose [nGy/s]	Detector Dose [nGy/s]
7	77.4 ± 15.4	100 ± 5.02	589	98 ± 1.3
30	62.8 ± 10.4	88.4 ± 4.42	522	na
50	63.0 ± 6.71	83.0 ± 4.15	483	na
100	73.3 ± 11.3	70.1 ± 3.51	411	84.2 ± 6.8
300	59.4 ± 8.63	45.3 ± 2.26	269	51.8 ± 2.9
1000	36.3 ± 3.66	19.4 ± 0.97	110	44.7 ± 2.5

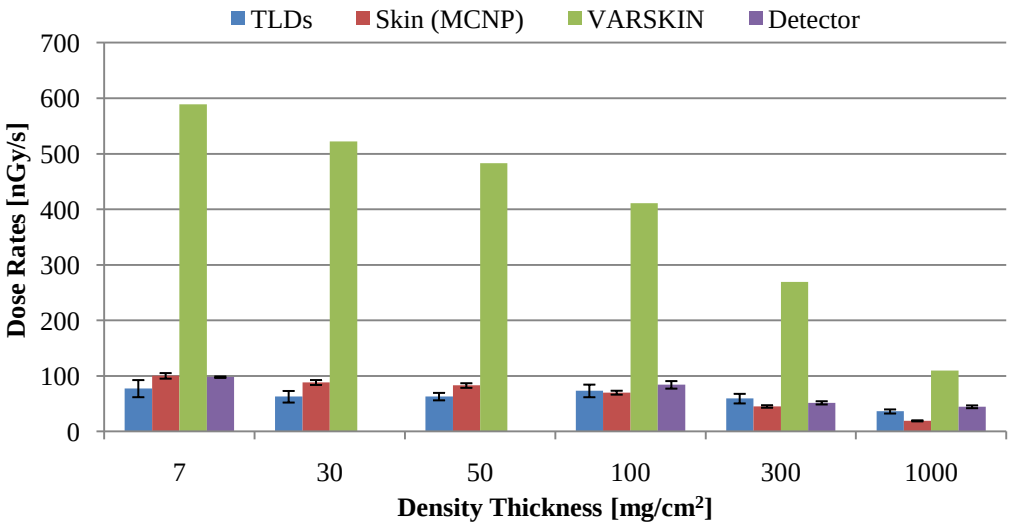

Figure 8-4: Ba-133 result comparison

VARSKIN version 3 does not account for the buildup region to charged particle equilibrium. It only uses KERMA as it assigns dose; therefore, it reports higher doses

in the shallow dose region. VARSKIN version 4 corrects for this and may yield lower results. VARSKIN version 4 is currently under development. Also, the Ba-133 source was modeled as a point source instead of a disk source due to VARSKIN version 3 restraints. A point source will yield higher results than a disk source. The data for the TLDs, MCNP skin model, and the prototype detector match extremely well for all the layers.

Table 8-10: Sr-90 results comparison

Sr-90/Y-90 Layer [mg/cm^2]	TLDs Dose [nGy/s]	MCNP (Skin) Dose [nGy/s]	VARSKIN Dose [nGy/s]	Detector Dose [nGy/s]
7	36.2 ± 11.0	50.1 ± 2.51	39	34 ± 2.9
30	34.5 ± 11.4	32.4 ± 1.62	21	na
50	13.8 ± 5.52	24.45 ± 1.21	15	na
100	16.4 ± 5.72	15.2 ± 0.76	9	12.0 ± 2.9
300	4.49 ± 0.48	4.48 ± 0.22	3	2.6 ± 1.2

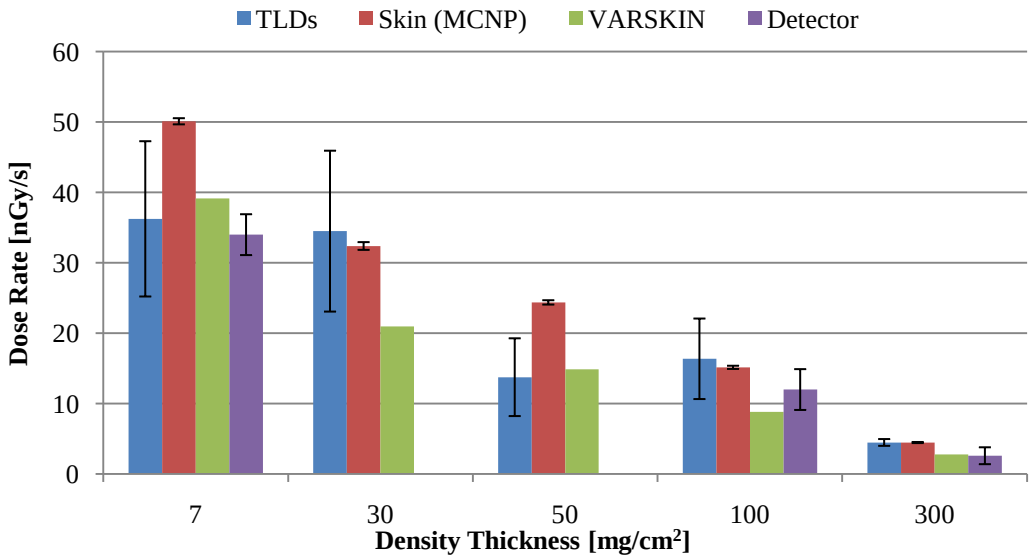

Figure 8-5: Sr-90 result comparison

The Sr-90 source results were close for all four methods. More accurate results could be obtained with specific measurements of the Sr-90 foil source.

9.0 Conclusions

The application of very thin TLD chips for determining dose rates at different depths in the skin was successful despite the inherent statistical variation of the TLDs. Based on the Sr-90 and Ba-133 results the prototype detector is functioning accurately; however, the other sources did not display as promising results.

The prototype detector responded close to the TLD results for the Cs-137 source at the 1000 mg/cm^2 layer. At the 100 mg/cm^2 layer the TLD results are about half of the reported results for the detector and the MCNP skin. This difference could be attributed to the use of two calibration curves for the Cs-137 source. The expected dose for the 100 mg/cm^2 falls within the saturation region of the chip and consequently where the two calibration curves would intersect. A more detailed calibration curve could be constructed to determine exactly where the TLD chip saturation is occurring to better determine the multiple calibration lines.

The Co-60 results for shallow dose matches for all four methods; however, the TLD results are slightly higher at the deeper depths. This could be caused by the TLD saturation when developing the calibration curve. The calibration curve does not appear to display saturation; however, finer increments may reveal a saturation point. Further research is also required to determine the difference between the MCNP expected TLD chip dose to the experimental data for the Co-60 source. The expected MCNP results match the TLD chip results up to the density thickness of 100 mg/cm^2. The density thicknesses of 300 mg/cm^2 and 1000 mg/cm^2 do not agree, prompting further investigation into the calibration curves. Again the possible solution would be to redo the calibration curve with more increments to determine if a saturation point is observed. If such a phenomenon is occurring then a different calibration fit maybe required i.e. two linear lines, such as with Cs-137.

To obtain more accurate results each TLD chip could be individually measured to determine the exact mass of the chip. Measuring several TLDs yielded a ± 20 μm tolerance in the TLD chip thickness. This difference in thickness would affect the

mass of the chip and therefore the reported dose. This approach would be very tedious and would require delicate handling of the TLD chips.

The TLD chip results are modified to obtain a 1 mg/cm^2 thick region that has a surface area 10 cm^2, which is facing the source. The scintillator thicknesses in the prototype detector are on the order of 20 mg/cm^2 and 60 mg/cm^2, depending upon the type and position of the scintillators. This difference in density thickness will affect the results. The object of this research was to determine the dose rate at various depths in the skin, with each skin region being 1 mg/cm^2 with 10 cm^2 of area. This was accomplished and with the data available in this research a comparison to 20 mg/cm^2 or 60 mg/cm^2 is possible.

The C-14 difference between the MCNP skin results and the TLD results are believed to be attributed to the very low beta energy of C-14 and the post-irradiation annealing procedure. The post-irradiation anneal was performed the same for every chip regardless of the type of source used to minimize possible variables in the results. The post-irradiation anneal is standard practice for TLD analysis and is used to remove low energy electron traps within the crystal. The low energy beta particles may be contributing to these low energy traps within the crystal due to lack of energy to produce a prominent peak on a glow curve output. The post-irradiation anneal may be removing part of the low energy beta signal, therefore reducing the signal output for the TLD chip. Further research would be required to determine if the post-irradiation anneal is indeed affecting the C-14 exposed TLD chip signals. Also, the results from the prototype detector suggests that the C-14 source specifications are not correct and that a thinner source window is more probable than the information obtained from the manufacturer.

The calibration curve is the most important component of the research. The calibration curve relates a known delivered dose to the TLD output. The output of a TLD reader is specific to that TLD reader. Calculation of the known delivered dose for the calibration curves is also vital. This calculation is heavily dependent upon how

the radioactive source is modeled and what assumptions are made when modeling. In this research, attention to detail when modeling the radioactive sources was paramount.

This research obtained the dose rates at the desired skin depths and validated the prototype detector. The prototype detector thus far proves to be a possible detection method and merits further development.

10.0 Future Work

Additional research should be performed on the thin TLD chips to better grasp the chip's characteristics. The saturation region on the thin TLD chips for different nuclides should be established to better develop calibration curves.

Greater accuracy and statistics is obtained with more data points. Additional increments on the calibration curve could be implemented, as well as increasing the number of TLD chips per cluster. Currently, 5 TLD chips were irradiated per data point: increasing that quantity to 20 would significantly increase the accuracy and statistics of the final data point.

A TLD reader capable of glow curve outputs could allow the possibility of beta and gamma discrimination. Analyzing the glow curve output by peak magnitude and location comparisons may yield individual beta and gamma signals. This could provide valuable information at specific layers in the skin without the need to add a filter to the source to eliminate the beta particles, since this method results in attenuation of the gamma particles as well.

Dose rates to various depths of the skin with the addition of protective clothing could be determined for both solid sources and liquid sources. This would provide experimental data through multiple layers of attenuation, which is more likely to occur in industry where protective clothing is worn in contamination areas.

A similar experiment using Radiochromic films is being conducted at Oregon State University. A comparison of the TLD against the Radiochromic film should be completed. The Radiochromic has several advantages: (1) greater sensitivity, (2) tissue equivalent, (3) extremely thin active layers, (4) ease of processing, and (5) ability to cut different sizes of film.

Liquid sources could be attempted again. Liquid sources allow for non-uniform irradiations with minimal attenuation of the source; therefore, providing the closest approximation to hot particles found in industry. The use of a liquid source would

require either a more precise pipette dispenser for volumes of less than 1 µL; however, this approach is going to take a long period of time (months) and is rather expensive for the cost of a pipette dispenser. A second approach would be to alter the chemistry of the liquid solutions to achieve a uniform distribution. This approach would require a great deal of additional research and experimental work with the chemical solutions.

11.0 Bibliography

23391, 5. F. (1991). *10CFR20: Energy, Standards for Protection Against Radiation.* Nuclear Regulatory Commission . Office of the Federal Register.

Brock, K. M. Oregon State University Radiation Center Health Physics Procedures (2001). *RCHPP 15: Operating Procedures for the Environmental Thermoluminescent Dosimetry (TLD) Program*.

Carron, N.J. (2007). *An Introduction to the Passage of Energetic Particles through Matter*. New York: Taylor & Francis Group.

Cazalas, E. "Design, Construction, and Analysis of a Skin Contamination Dosimeter". Master's Thesis. November 2009.

Cember, H., T. E. Johnson (2009). *Introduction to Health Physics*. New York: McGraw Hill.

Charlesby, A. (1965). Solid-state polymerization induced by radiation. Reports on Progress in Physics, 28, 463 – 518.

DOE ORNL/CP-95027, Department of Energy, Beta Reduction Factors For Protective Clothing At The Oak Ridge National Laboratory, Oak Ridge, Tennessee; 1997.

Gad, Shani (1991) *Radiation Dosimetry: Instrumentation and Methods*. Ann Arbor: CRC Press.

International Commission on Radiological Protection. ICRP 38: Decay Schemes.

International Commission on Radiological Protection. (1991). *ICRP 59: The Biological Basis for Dose Limitation in the Skin* (Vol.22 No.2) Oxford: Pergamon Press.

International Specialty Products, Gafchromic EBT Self-Developing Film for Radiotherapy Dosimetry; August 2007.

Knoll, G. F. (2000). *Radiation Detection and Measurement* (3rd Ed). Hoboken, NJ: John Wiley & Sons, Inc.

Los Alamos National Laboratories. (2003). MCNP5. Oak Ridge, TN: Radiation Safety Information Computational Center.

Martin, J. E. (2006). *Physics for Radiation Protection* (2nd Ed). Wiley-VCH.

McMaster Carr. (2009). Retrieved from http://www.mcmaster.com

National Council on Radiation Protection and Measurements. (1999). NCRP Report No. 130: Biological Effects and Exposure Limits for Hot Particles. Bethesda, MD.

National Institute of Standards and Technology. Composition of Tissue. Retrieved from http://physics.nist.gov

National Nuclear Data Center. Chart of the Nuclides. Retrieved from Brookhaven National Laboratory: http://www.nndc.bnl.gov/char/

Niroomand-Rad, A., Blackwell, R.C., & Coursey, B. M. (1998). Radiochromic film Dosimetry: Recommendations of AAPM Radiation Therapy Committee Task Group 55. Medical Physics, 25 (11), 2093 – 2115.

Reynaert, N., Jeraj, R. (2002). Parameter dependence of the MCNP electron transport in determining dose distributions. Medical Physics, 29 (10), 2446-2454.

Shultis, Kenneth J., Richard E. Faw, Fundamentals of Nuclear Science and Engineering. New York: Marcel Dekker, Inc., 2002.

ThermoFisher. (2009) Retrieved from http://thermofisher.com

Thuo, K. "Photon Skin Dosimetry at Depth". Master's Thesis (In Progress)

Turner, J. E. (2007). *Atoms, Radiation, and Radiation Protection* (3rd Ed). Wiley-VCH.